ICT-619555 RESCUE

D1.4 Version 1.0

Intermediate Results of Wireless Access and Multiple Antennas Technologies

Contractual Date of Delivery to the CEC: *M12*
Actual Date of Delivery to the CEC:

Editor	Maximilian Matthé
Author(s)	Maximilian Matthé, Meng Cheng, Jiancao Hou, Na Yi, Matsumoto Tadashi
Participants	TUD, JAIST, UNIS
Work package	WP1 - Theoretical analyses for limit and rate-disortion region
Security	**CO**
Nature	**R**
Version	1.0
Total number of pages	49

Abstract: In this deliverable intermediate results on multiple access and multiple antenna technologies for RESUE are described. We start with an introduction summarizing the requirements on the physical layer and multiple access technologies. The main part is dedicated to non-orthogonal multiple access, where we investigate the suitability of GFDM and IDMA for RESCUE requirements. We can show that both techniques are suitable for RESCUE. Initial considerations are carried out, how GFDM and IDMA can be combined to combine the benefits of both schemes. Furthermore, we describe a reduced-complexity algorithm for solving the power distribution for coordinated beamforming in a multi-relay scenario. It is shown that the described algorithm outperforms existing algorithms in terms of computational complexity and convergence speed.

Keyword list: unpredictable environment, multiple access, multi-antenna technologies, generalized frequency division multiplexing, interleaved division multiple access, coordinated beamforming

Executive Summary

This deliverable contains the description of current research status on multi-antenna and multiple access (MA) schemes for the considered RESCUE scenarios. Initially, a summary of the requirements posed by the RESCUE scenarios on the employed waveform and MA scheme is given. Most important are robustness against asynchronicity and unpredictable environments, but also flexibility and latency need to be considered. Then, carrier sense multiple access with collision avoidance (CSMA/CA) is shortly introduced as it is the MA scheme which is considered for implementation in RESCUE WP3.

Afterwards, we emphasize on non-orthogonal MA schemes being researched under RESCUE. In particular, the non-orthogonal waveform generalized frequency division multiplexing (GFDM) is considered as a promising candidate for RESCUE scenarios. Baseband algorithm for GFDM are described in detail and is shown to outperform orthogonal frequency division multiplexing (OFDM) in simulations. We also investigate dedicated MA schemes that can be used with GFDM. There, it is shown that frequency-division multiple access (FDMA) and CSMA/CA directly work out-of-the-box. Additionally, space-time-coding for GFDM is described in order to improve the robustness against mobility fading.

As a non-orthogonal MA scheme, interleaver-division multiple access (IDMA) is described in detail. It is shown that IDMA can reach higher spectral efficiency than conventional orthogonal MA schemes such as FDMA or time-division multiple access (TDMA). However, this comes at the price of increased computational complexity when applying the multi-user detection (MUD) algorithm for IDMA. Furthermore, initial considerations on how GFDM can be combined with IDMA to benefit from both approaches are described.

Finally, we study multi-relay coordinated multiple-input multiple-output (MIMO) beamforming as a mean to reduce power when relays are serving several users. A reduced complexity algorithm for the computation of beamforming vectors is also provided in this document. Our solution outperforms previous algorithms in terms of computation convergence and calculation speed. It is shown that the proposed beamforming algorithm provides equal beamforming vectors as previously published algorithms, however, with significantly reduced complexity.

The work in this deliverable directly contributes to the required RESCUE gains, which are increase in spectral efficiency and capacity, reduced outage probability and transmit power reduction. With the adoption of non-orthogonal waveforms, we can increase the point-to-point spectral efficiency. Non-orthogonal multiple access increases overall system capacity and spectral efficiency compared to conventional orthogonal multiple access schemes. With the application of transmit diversity per link, the transmit power and outage probability is reduced. Further, by application of coordinated beamforming, both spatial diversity is exploited and outage probability is reduced. This deliverable only describes intermediate research results regarding these topics. Final evaluation is to be carried out in RESCUE D1.3.

Authors

Partner	Name	Phone/Fax/e-mail
Technical University Dresden (TUD)	Maximilian Matthé	Phone: +49 351 463 41071 Fax: – EMail: maximilian.matthe@ifn.et.tu-dresden.de
University of Surrey (UNIS)	Jiancao Hou Na Yi	EMail: jiancao.hou@surrey.ac.uk EMail: n.yi@surrey.ac.uk
Japan Advanced Institute of Science and Technology (JAIST)	Meng Cheng Matsumoto Tadashi	EMail: chengmeng@jaist.ac.jp EMail: matumoto@jaist.ac.jp

Table of Contents

List of Acronyms and Abbreviations

Term	Description
5G	5th generation
ACK	Acknowledgement
AWGN	Additive white Gaussian noise
BER	Bit error rate
BFDM	Bi-orthogonal frequency division multiplexing
BICM-ID	Bit-interleaved coded modulation with iterative detection
BS	Base station
CA	Collision avoidance
CDMA	Code-division multiple access
CFO	Carrier frequency offset
CHADE	Chained detection
CP	Cyclic prefix
CSI	Channel state information
CSMA/CA	Carrier sense multiple access with collision avoidance
CSMA	Carrier sense multiple access
CS	Cyclic suffix
CTS	Clear-to-send
DACC	Doped accumulator
DFT	Discrete Fourier transform
E2E	End-to-end
EBSA	EXIT-constrained binary switching algorithm
EM	Extended mapping
ESE	Elementary signal estimator
EXIT	Extrinisic information transfer chart
FBMC	Filterbank multicarrier
FDMA	Frequency-division multiple access
FEC	Forward error correction
FSCs	Frequency-selective channels
FSC	Frequency-selective channel
FT	Fourier transform
GFDMA	Generalized frequency division multiple access
GFDM	Generalized frequency division multiplexing
ICI	Inter-carrier interference
IDMA	Interleaver-division multiple access
ISI	Inter-symbol interference
IUI	Inter-user-interference
LOS	Line-of-sight
LOTF	Links-On-The-Fly
LTE	Long Term Evolution
M2M	Machine-to-machine
MAC	Medium access control
MAI	Multiple access interference
MA	Multiple access
MF	Matched filter
MIMO	Multiple-input multiple-output
MI	Mutual information
MM	Modulation mixing
MRC	Maximum ratio combiner
MSE	Mean squared error
MUD	Multi-user detection
NEF	Noise enhancement factor
NLOS	Non line-of-sight

NOMA	Non-orthogonal multiple access
OFDM	Orthogonal frequency division multiplexing
OOB	Out-of-band
PHY	Physical layer
PN	Pseudo-noise
PTT	Push-to-talk
QAM	Quadrature amplitude modulation
RC	Raised cosine
RF	Radio frequency
RRC	Root raised cosine
RSs	Relay stations
RS	Relay station
RTS	Request-to-send
SC-FDE	Single-carrier frequency domain equalization
SDP	Semidefinite programs
SER	Symbol error rate
SINR	Signal-to-interference-and-noise-ratio
SISO	Single-input single-output
SLNR	Signal to leakage plus noise ratio
SNR	Signal to noise ratio
SPC-IrR	Single parity check and irregular repetition
SPC	Single-parity check
SSIC	Soft successive interference cancellation
STC	Space-time coding
STO	Symbol timing offset
SUD	Single-user detection
TDMA	Time-division multiple access
TR-STC	Time-reversal space-time code
UCA	Uniform circular array
UFMC	Universal filtered multicarrier
ULA	Uniform linear array
V2V	Vehicle-to-vehicle
WLAN	Wireless local area network
ZF	Zero-forcing

1. Introduction

The focus of research in RESCUE lies in the development of robust technologies for data transmission over networks in an unpredictable environment. There, the concept of Links-On-The-Fly (LOTF) aims at increasing network capacity and reducing outage probability by letting relay nodes forward frames even if they cannot decode it correctly. At the destination, the receiver needs to cope with decoding several, possibly erroneous, copies of the same message and to estimate the original, error-free message.

Another important aspect in designing a robust end-to-end (E2E) data transmission over wireless networks is how nodes communicate with each other in the physical layer (PHY) in general and, in particular, how coded bits are transmitted from one node to another. In principle, this can be built on top of the PHY of Long Term Evolution (LTE) or wireless local area network (WLAN). However, consideration of waveforms addressing the specific requirements of RESCUE application scenarios is an important aspect.

Furthermore, with the LOTF technology, messages are expected to be transmitted by several copies from several relays to the destination, increasing the load on the medium access control (MAC) layer to allocate resources for each transmission. Therefore, the investigation of advanced multiple access (MA) schemes providing an efficient distribution of radio frequency (RF) resources to different nodes is another important aspect of the research in RESCUE.

1.1 Requirements on Physical Layer

In a previous research step, RESCUE applications scenarios have been developed [D11]. There, a public safety and a vehicle-to-vehicle (V2V) use case have been defined and functional requirements of the PHY were established. In summary, the following features of a new PHY are required for the RESCUE scenarios:

Robustness against asynchronicity The constantly changing topology within the RESCUE scenarios cannot ensure a synchronous operation of all nodes within the ad-hoc network. Therefore, frequency and timing misalignments are likely to appear between several nodes. Furthermore, source and destination can have a constant difference in frequency, i.e. carrier frequency offset (CFO) occurs. A robust PHY is required to cope with these impairments in an efficient way.

Simultaneous access of users The transmission of several, copies of a message over multiple routes strongly increases the load on the network. Since erroneous messages are not necessarily dropped, network load is even further increased with the LOTF concept. Hence it is strongly required that the RESCUE MA protocol allows several nodes to simultaneously transmit on a shared time-frequency resource in order to not increase transmit latency.

Low latency transmission In RESCUE scenarios there exist several timing-critical messages that need to be delivered within a certain delay. For example, in the V2V use case, messages for the electronic break light or accident alarms need to be delivered as fast as possible. Also, in public safety use cases, latency can become an issue, e.g. in the push-to-talk (PTT) communication case. Therefore, both the RESCUE PHY waveform as well as the MA technique need to consider latency as a performance metric.

Spectral efficiency Spectral efficiency is a main point for any wireless transceiver scheme as a low spectral efficiency increases delays and network load or required bandwidth. RESCUE is therefore also considering spectral efficiency as a performance indicator.

Robustness against fading and dispersive wireless channels Especially with the non-stable changing network topology and node mobility, channel fading becomes an issue for the PHY waveform. Severe multipath effects are expected in urban areas and with high mobility, wireless channels can become fast faded and even frequency-dispersive as is shown in [AI07]. A suitable transceiver scheme for RESCUE needs to be robust against these types of fading and provide means to equalize channel effects. For example, multi-antenna techniques and distributed coding provide means for exploiting channel diversity to increase the robustness against dispersive channels.

Flexibility to adapt to channel quality Within RESCUE, a rate adaptation protocol will be developed. Hence, a

suitable RESCUE PHY needs to be able to adapt the modulation and coding schemes to the quality of the channel. This can be achieved by either changing modulation or the code rate and needs to be supported by the waveform and coding algorithms. Another considerable aspect is, if the PHY can adapt itself to different channel conditions by changing physical parameters such as pulse shaping filters, bandwidth or subcarrier distance.

It is notable, that the presented requirements overlap with the requirements proposed for the PHY of 5th generation (5G) networks [WJK+14; FA14; Fet14]. In particular, spectral efficiency, low latency and imperfect synchronization are important aspects in the development of 5G PHY. As in 5G networks, machine-to-machine (M2M) traffic will be significantly increased [DGK+13], random access and the possibility to serve a massive number of users is a key point for multiple access techniques in 5G PHY. In the process of research, strict orthogonality of underlying waveforms is critically questioned, and the latest research considers non-orthogonal waveforms and multiple access schemes to cope with the requirements of future networks [WJK+14].

1.2 Contribution of this Deliverable

The goal of this deliverable is the reporting of current state of reasearch on MA and multi-antenna techniques within RESCUE. Since the research is still ongoing, according to the project proposal only intermediate results are shown.

Within research for 5G networks, several new waveforms are explored [WJK+14]. In particular, filterbank multicarrier (FBMC) [IVS+10], universal filtered multicarrier (UFMC) [WSC14], bi-orthogonal frequency division multiplexing (BFDM) [KWJ+14] and generalized frequency division multiplexing (GFDM) are promising candidates that are being researched in the EU project 5GNOW [WKB+12]. Within RESCUE it is examined, how GFDM can cope with the specified requirements. Furthermore, we investigate how GFDM can be extended by a multiple access technique and how this fits into the RESCUE system structure. The description of GFDM and its possibilities for adaptation of multiple access techniques is provided in Sec. 2.1 of this document.

Another contribution of this deliverable resides in the investigation of the compatibility of interleaver-division multiple access (IDMA) with RESCUE scenarios. We consider IDMA to be a promising technique due to its ability of coping with severe user asynchronicity and its increased spetral efficiency compared to conventional MA schemes. Furthermore, with IDMA no scheduling is necessary since every user is only identified with its used interleaver and each user can send a data block at any time. By using extended mapping and multi-user detection, IDMA can achieve performance very close to the Shannon limit of a wireless channel. The details of IDMA are described in Sec. 2.2 of this deliverable.

The distribution of transmit powers for coordinated beamforming in a multi-relay multi-user scenario as it appears in RESCUE requires to solve the max-min signal-to-interference-and-noise-ratio (SINR) problem. Even though algorithms for this problem exist, they are computationally complex due to their slow convergence within iterations. This deliverable contributes a modified algorithm for the max-min SINR problem that converges significantly faster and hence can reduce the power consumption and delays in the relay network. The detailed motivation and algorithm description is contributed in Sec. 3.

Ongoing research in RESCUE WP3 has decided to use carrier sense multiple access with collision avoidance (CSMA/CA) and time-division multiple access (TDMA) as the multiple access technique used for implementation to demonstrate the LOTF concept. Therefore, the general principle of carrier sense multiple access (CSMA) is shortly described in Sec. 1.3. Additionally, Sec. 2.1 describes how CSMA can be combined with GFDM. But also non-orthogonal multiple access schemes such as IDMA have been shown to provide a higher sum rate and hence higher spectral efficiency in a multi-user environment. Therefore, Sec. 2.3 describes initial considerations on the combination of the non-orthogonal waveform GFDM with the non-orthogonal MA scheme IDMA. Potential benefits and problems are identified and an initial system structure is proposed.

1.3 Carrier Sense Multiple Access with Collision Avoidance (CSMA/CA)

A MA technique is required for any system involving several nodes that share one physical medium. The MA protocol defines, which node uses which resource on the medium at a particular time. Its task is to distribute the

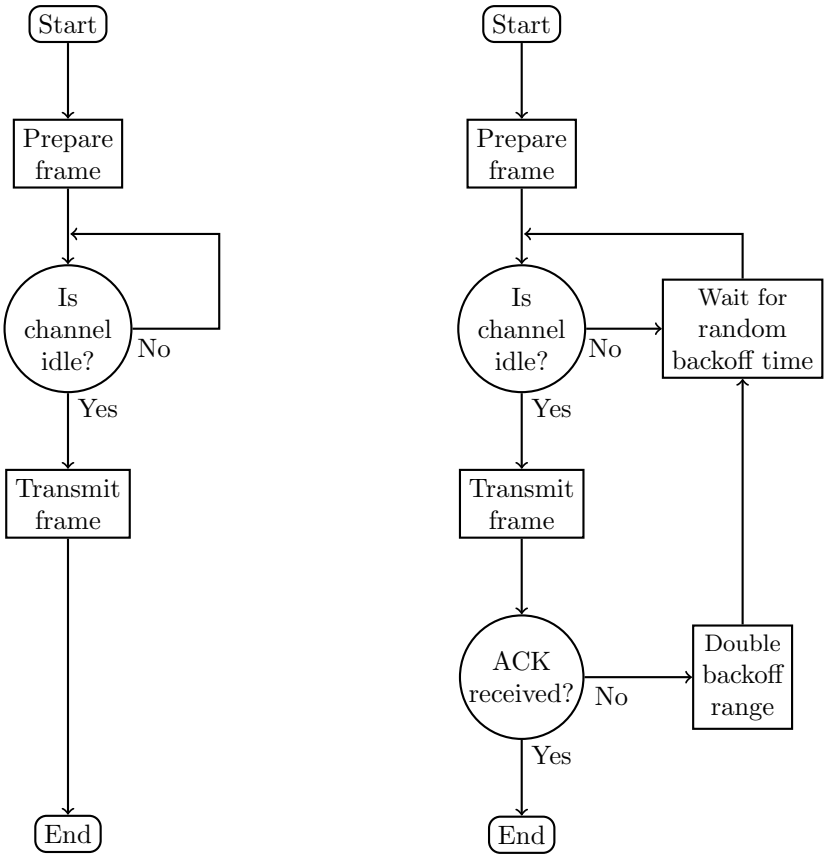

(a) CSMA (b) CSMA/CA

Figure 1.1: Algorithm flow for CSMA and CSMA/CA.

resources so that every node can transmit and receive the data it needs. Furthermore, achieving fairness in the access to the shared resources is an essential role of access techniques. In literature several MA techniques exist [TM00], where non-orthogonal multiple access (NOMA) techniques [DYF+14] are very promising for unreliable and unpredictable environments. NOMA schemes that are researched for RESCUE are treated in detail in Chapter 2. However, these schemes tend to be very complex regarding prototyping efforts and hence, they are only examined in simulations and theoretic considerations. The prototype of the RESCUE project will use a MA technique named CSMA/CA [HHS+09]. The fundamental properties of CSMA/CA scheme are described in the following, whereas the required modifications specific for RESCUE scenarios are treated in detail in RESCUE Deliverable D3.1.

As the RESCUE system can be both centralized and decentralized, in general the MA technique cannot rely on a central scheduler that distributes transmission resources to the nodes. With the packet-switching MA scheme CSMA/CA, every node can access the physical channel autonomously without requiring information from a central control unit. The CSMA technique can be summarized by the simple "listen-before-talk" principle, but is explained in more detail below.

Simplified algorithm flow diagrams for CSMA and CSMA/CA are shown in Fig. 1.1. In conventional CSMA, before using the physical channel, each node senses the channel if it is idle and currently not used. Hence, the transmitter requires feedback from the receiver of the node to determine if currently a transmission from another node is occuring on the channel. In case the channel appears unused, the node immediately transmits its data. In case the channel appears to be used, the node waits until the channel becomes idle and then immediately transmits its frame.

Several drawbacks arise with this approach. First, in pure CSMA, no collisions can be detected. It is assumed,

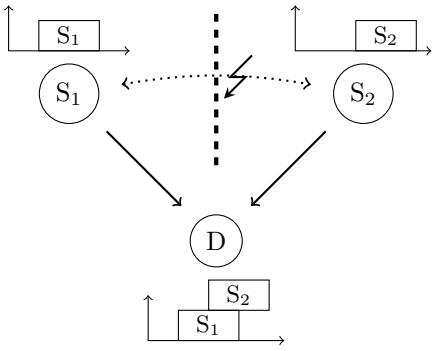

Figure 1.2: Hidden node problem with CSMA.

that collisions do not occur since the medium is sensed to be idle before transmission. However, in wireless environments, the propagation delay between nodes renders this assumption incorrect. Additionally, all waiting nodes start transmission as soon as the medium gets free, making collisions very likely to happen in highly loaded scenarios. Another drawback comes with the hidden node problem in wireless environments (Fig. 1.2). Both sources S1 and S2 want to transmit data to the destination D. However, they cannot hear each other and hence assume the channel at the destination is free. Consequently, a collision happens at the destination and both sources need to retransmit their data, since the destination cannot provide an acknowledgement (ACK).

CSMA/CA addresses the mentioned drawbacks by adding an acknowledgement protocol to detect, if a collision at the receiver occured and introducing a delay after a channel use has been recognized. The node only again tries to access the channel after this delay has passed. This way, as soon as the channel becomes idle, not every node transmits at the same time, but the one with the smallest delay starts, hindering the others to use this slot. Hence, collisions can be significantly avoided [DDT09]. Furthermore, the hidden-node problem is addressed in CSMA/CA by the introduction of request-to-send (RTS) and clear-to-send (CTS) messages.

In case a collision appears in CSMA/CA which is detected by a missing ACK, nodes wait for a random time within their wait backoff. If multiple collisions for the same frame appear, the backoff is increased exponentially with each collision. This way, packet bursts are dilated in time and recurring collisions are avoided. The necessary extensions to CSMA/CA for RESCUE scenarios are discussed within RESCUE Deliverable D3.1.

2. Nonorthogonal Multiple Access Schemes for RESCUE

In this section first generalized frequency division multiplexing (GFDM) is introduced and it is described, how it can be combined with a MA scheme that is suitable for RESCUE scenarios. Furthermore, interleaver-division multiple access (IDMA) is discussed and presented as a promising candidate for non-orthogonal multiple access (NOMA) with increased spectral efficiency. Finally, it is considered how GFDM and IDMA can be combined to benefit from the advantages of both systems.

2.1 Generalized Frequency Division Multiple Access

This section describes GFDM as a waveform which is suitable for the PHY of systems operating in RESCUE scenarios. Initially, the transceiver is introduced and core concepts like channel estimation, synchronization, and multi-antenna techniques for GFDM are described. MA techniques are described that can be combined with GFDM to serve several users on the same wireless channel, leading to generalized frequency division multiple access (GFDMA). Finally, system performance is analyzed theoretically and by simulations.

2.1.1 GDFM system description

The block diagram of the GFDM transceiver for a single user is provided in Fig. 2.1. The binary data vector $\vec{b}$ is encoded by a generic encoder to obtain $\vec{b}_c$ and further mapped to complex-valued constellation symbols $\vec{d}$, which can for example be taken from a 2^{μ} quadrature amplitude modulation (QAM) constellation, where μ is the number of bits per constellation point. $\vec{d}$ contains $N = KM$ elements, which are distributed onto M subsymbols, where each subsymbol transmits K different subcarriers according to

$$\mathbf{D} = \begin{pmatrix} \vec{d}_0 & \vec{d}_1 & \dots & \vec{d}_{M-1} \end{pmatrix} \qquad \text{and} \qquad \vec{d}_m = \begin{pmatrix} d_{0,m} & d_{1,m} & \dots & d_{K-1,m} \end{pmatrix}^T. \tag{2.1}$$

$\mathbf{D}$ represents $\vec{d}$ distributed onto K subcarriers and M subsymbols, $\vec{d}_m$ contains the data symbols that are to be transmitted in the mth subsymbol and $d_{k,m}$ describes the constellation symbol transmitted on the kth subcarrier and mth subsymbol. Note that $\vec{d} = \mathrm{vec}(\mathbf{D})$, where $\mathrm{vec}(\mathbf{X})$ denotes the stacking of the columns of the matrix $\mathbf{X}$ on top of each other.

Fig. 2.2 illustrates the details of the GFDM modulator. A prototype pulse $g[n]$ is circularly shifted in time and frequency to the kth subcarrier and mth subsymbol, yielding $g_{k,m}[n]$ given by

$$g_{k,m}[n] = g\left[(n - mK) \mod N\right] \cdot \exp\left[-j2\pi \frac{k}{K} n\right], \tag{2.2}$$

with n denoting the sampling index. $g_{k,m}[n]$ is then applied to transmit the constellation symbol $d_{k,m}$. Finally, the complete transmit signal $x[n]$ of a GFDM block is given by the summation over all transmitted symbols

$$x[n] = \sum_{k=0}^{K-1} \sum_{m=0}^{M-1} g_{k,m}[n] d_{k,m}, \quad n = 0, \dots, N-1. \tag{2.3}$$

The linear equation (2.3) can be reformulated to a matrix equation

$$\vec{x} = \mathbf{A}\vec{d}, \tag{2.4}$$

where $\mathbf{A}$ is a $KM \times KM$ transmitter matrix [MKL+12] with a structure according to

$$\mathbf{A} = \begin{pmatrix} \vec{g}_{0,0} & \dots & \vec{g}_{K-1,0} & \vec{g}_{0,1} & \dots & \vec{g}_{K-1,M-1} \end{pmatrix} \tag{2.5}$$

where $\vec{g}_{k,m} = (g_{k,m}[n])_n$ are column vectors containing the samples of $g_{k,m}[n]$ for $n = 0, \dots, N-1$ and $\vec{x} = (x[n])_n$. After modulation, at the transmitter side a cyclic prefix of N_{CP} samples is added to produce $\tilde{\vec{x}}$.

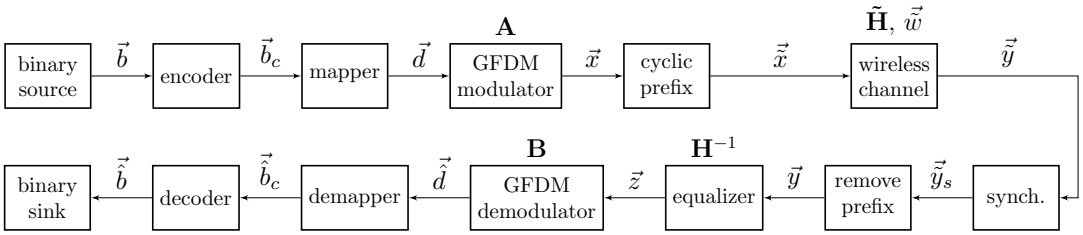

Figure 2.1: Block diagram of the GFDM transceiver [MMG+14b].

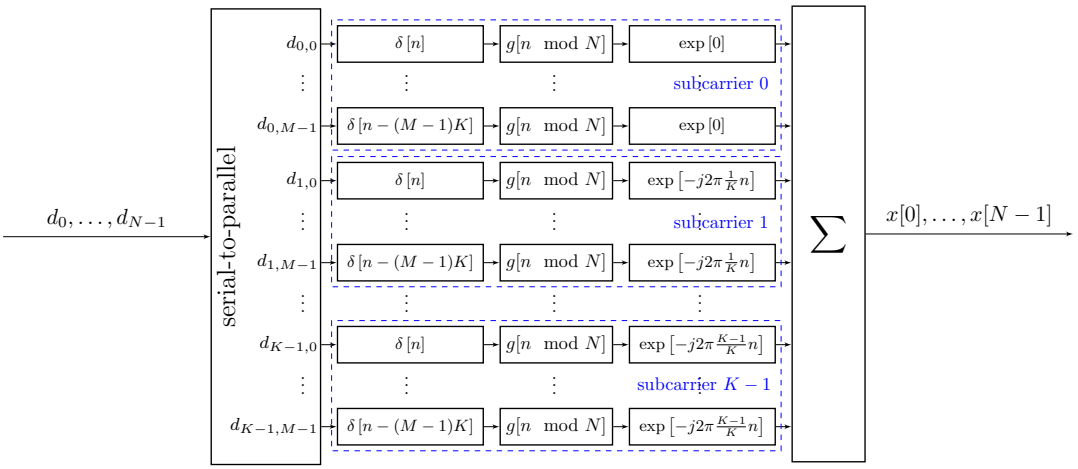

Figure 2.2: Details of the GFDM modulator [MMG+14b].

The received signal after transmission through a wireless channel is modeled by

$$\vec{\hat{y}} = \tilde{\mathbf{H}}\vec{\tilde{x}} + \vec{\tilde{w}}, \tag{2.6}$$

where $\tilde{\mathbf{H}}$ is a band-diagonal Toeplitz matrix of size $N + N_{CP} + N_{ch} - 1 \times N + N_{CP}$ expressing a convolution with the channel impulse response $\vec{h}$ of length N_{ch} and $\vec{\tilde{w}}$ denotes the additive white Gaussian noise (AWGN) at the receiver. After time and frequency synchronization have been performed at the receiver yielding the signal $\vec{\tilde{y}}_s$, the cyclic prefix (CP) is removed to produce the signal $\vec{y}$. Assuming perfect synchronization, due to the use of the CP this whole process can be summarized by

$$\vec{y} = \mathbf{H}\vec{x} + \vec{w}, \tag{2.7}$$

where $\mathbf{H}$ is a circulant matrix that describes a circular convolution of the transmitted signal with the channel impulse response.

The use of a CP hence transforms the linear convolution with the channel impulse response into a circular. Since circulant matrices are diagonalized by the Fourier transform (FT), channel equalization can be efficiently achieved in the frequeny domain as it is the case for OFDM systems [Bin90]. Hence, the equalized GFDM signal is given by

$$\vec{z} = \mathbf{F}^H \frac{\mathbf{F}\vec{y}}{\mathbf{F}\vec{h}} = \vec{x} + \mathbf{F}^H \frac{\mathbf{F}\vec{w}}{\mathbf{F}\vec{h}} \tag{2.8}$$

$$\vec{z} = \mathbf{A}\vec{d} + \bar{\vec{w}} \tag{2.9}$$

where $\mathbf{F}$ denotes a normalized Fourier matrix and $\vec{h}$ is zero-padded to the correct length. $\bar{\vec{w}}$ denotes the colored noise after channel equalization. $\vec{z}$ is then sent to the GFDM demodulator which for each subcarrier performs a circular convolution with a subcarrier receiver filter and subsequent downsampling at the symbol timings. This procedure is most simply described by

$$\vec{\hat{d}} = \mathbf{B}\vec{z}, \tag{2.10}$$

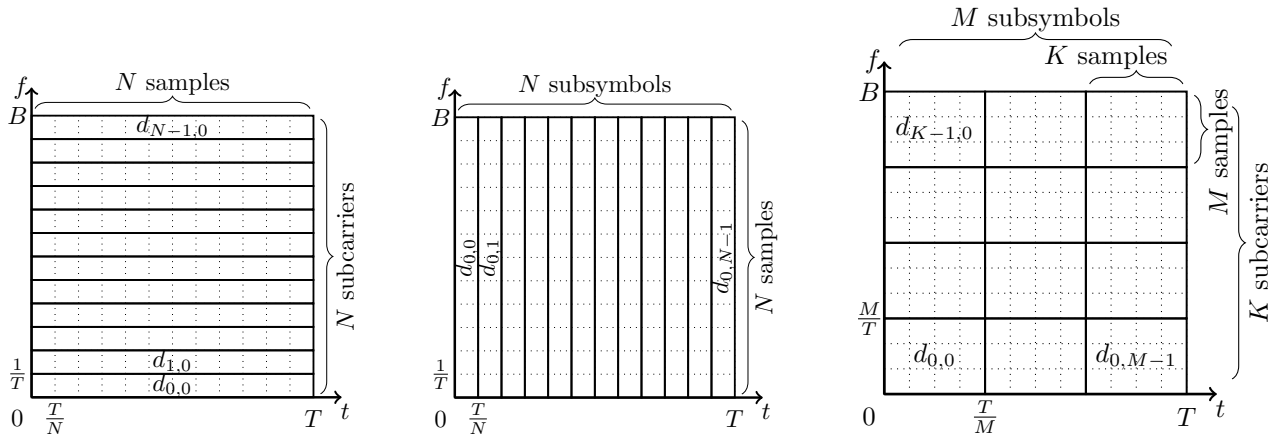

(a) OFDM **(b) SC-FDE** **(c) SC-FDM and GFDM**

Figure 2.3: Time-frequency partitioning of available resources for different schemes: (a) $K = N, M = 1$ **(b)** $K = 1, M = N$ **(c)** $K = 4, M = 3$ **[MMG+14b]**

where **B** contains the subcarrier filters as its rows. There are standard receiver types for GFDM readily available in literature: the matched filter (MF) receiver $\mathbf{B}_{MF} = \mathbf{A}^H$ optimizes the signal to noise ratio (SNR) per data symbol, however due to the non-orthogonality of transmitter filters it introduces self-interference between the data. On the other hand the zero-forcing (ZF) receiver $\mathbf{B}_{ZF} = \mathbf{A}^{-1}$ combats the self-interference by using bi-orthogonal filters at the receiver, however at the cost of increased noise enhancement. It was shown in [MMF14a] that certain configurations of K and M lead to singular transmitter matrices **A** for which no ZF receiver exists and MF receivers perform worse with these configurations. In particular it was shown that odd M are advantageous for the GFDM system performance. After GFDM demodulation, the estimated constellation symbols $\vec{\hat{d}}$ are demapped to bits $\vec{\hat{b}}_c$ which can be passed to a subsequent generic decoder to finally yield an estimate of the transmitted bits $\vec{\hat{b}}$.

GFDM can be considered as a generalization of both orthogonal frequency division multiplexing (OFDM) and single-carrier frequency domain equalization (SC-FDE) systems. Fig. 2.3 shows the relation between these three transceiver schemes in terms of data distribution in time and frequency. OFDM distributes its data only in the frequency domain whereas SC-FDE performs a time-spreading of the transmitted data. With GFDM, a more generic solution is proposed where data can be distributed in both time and frequency domains. GFDM reduces to OFDM for $M = 1$ and $g[n] = \frac{1}{\sqrt{K}}$ and to SC-FDE when $K = 1$ and $g[n]$ is the Dirichlet filter [MMG+14a]. This amplifies the great flexibility of the proposed GFDM scheme which can adapt its grid to different channel conditions and furthermore can adapt the employed filter to different requirements.

2.1.2 Synchronization for GFDM

Since in RESCUE scenarios strict synchronization and synchronicity between users cannot be afforded or achieved it is very important that the receiver of a GFDM block is able to estimate the symbol timing offset (STO) and CFO of the transmitter relative to the receiver. In this section we propose a simple synchronization method which is based on a specific GFDM preamble.

We focus on single-shot synchronization, meaning that data and synchronization information are transmitted altogether, allowing two devices to directly communicate with each other without exchanging synchronization information before data transmission. For this purpose, the algorithm proposed in [AKE08] will be evaluated and adapted for GFDM. The preamble consists of 2 GFDM subsymbols, where $d_{k,0}$ and $d_{k,1}$ are filled with the same pseudo-noise (PN) sequence, resulting in a signal composed with two identical halves.

To achieve very low out-of-band (OOB) radiation, both the preamble and the data block are multiplied by a window which pinches the block boundaries. This is illustrated in Fig. 2.4, where different pinching lengths N_{Wp} and N_{Wd} can be applied to preamble and data block which influences the emission mask.

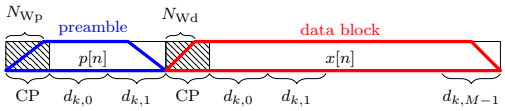

Figure 2.4: Windowed GFDM preamble preceding a windowed GFDM data block [MMG+14b].

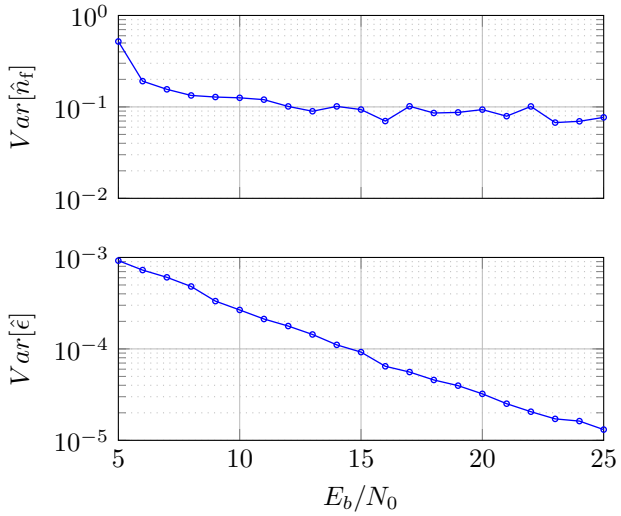

Figure 2.5: Simulated estimation performance of fine STO $\hat{n}_f$ and CFO $\hat{\varepsilon}$ for the GFDM preamble in a fading multipath channel [MMG+14b].

Let $r[n]$ be a set of received samples containing at least one complete GFDM preamble. Now, the two identical halves of the preamble are found by an autocorrelation metric. In order to remove the plateau which results from the CP and cyclic suffix (CS) usage, the metric is integrated with a moving window average filter [SC97], [MZB00], leading to the metric

$$\mu[n] = \sum_{\iota=-N_{\mathrm{CP}}}^{0} \sum_{k=0}^{N-1} r[n+\iota+k]^* r\left[n+\iota+k+\frac{N}{2}\right]. \tag{2.11}$$

A coarse STO estimate $\hat{n}_c$ is now given as the argument that maximizes $|\mu[n]|$:

$$\hat{n}_{\mathrm{c}} = \underset{n}{\mathrm{argmax}} |\mu[n]|, \tag{2.12}$$

and a CFO estimate $\hat{\varepsilon}$ is acquired from the angle of $\mu[\hat{n}_{\mathrm{c}}]$:

$$\hat{\varepsilon} = \frac{\arg \mu[\hat{n}_{\mathrm{c}}]}{\pi}. \tag{2.13}$$

Subsequently, the CFO is corrected with the help of $\hat{\varepsilon}$ and an auxiliary cross correlation metric $c[n]$ is calculated by

$$c[n] = \frac{1}{N} \sum_{k=0}^{N-1} r[n+k]^* e^{j2\pi \frac{\hat{\varepsilon}}{N}(n+k)} p[k], \tag{2.14}$$

where $p[k]$ represents the known GFDM preamble. Side peaks that arise in $c[n]$ due to the CP and CS of the preamble are compensated by jointly considering $c[n]$ and $\mu[n]$ to provide a more accurate STO estimate given by

$$\hat{n}_{\mathrm{o}} = \underset{n}{\mathrm{argmax}} \left(|c[n]||\mu[n]| \right). \tag{2.15}$$

Fig. 2.5 presents the estimation performance of normalized STO and CFO with a GFDM preamble that follows the parameters from Tab. 2.3, except for $M = 2$. A raised cosine (RC) window function with rollof length 16 is used

and the time-variant frequency-selective channel (FSC) is set as described in Sec. 2.1.4. The figure shows that the STO estimation becomes stable within tenths of a sample in higher SNR ranges above 5 dB. CFO can be estimated with an accuracy between 10^{-3} and 10^{-5} depending on the SNR.

The applied double-pinching configuration for the GFDM preamble shows that single-shot burst synchronization can be achieved without performance degradation compared to the results in [AKE08]. Furthermore, with the presented approach, OOB radiation is kept low by the application of the windowing above the GFDM block and preamble, which is an important aspect in particular in unpredictable and asynchronous operation of several users.

2.1.3 Channel Estimation for GFDM

The previous section has shown a technique to synchronize user and access point with an extra GFDM preamble. Within this section, time and frequency misalignment is considered as a part of a time-variant channel and can therefore be equalized by estimating the channel with a piloting structure [MMF15]. The presented approach is able to compensate the residual timing and frequency misalignment that results from the synchronization approach presented earlier.

We assume a system with the parameters from Tab. 2.3 where only half of the subcarriers are allocated with a user and the access point has a constant time misalignment $\Delta\tau$ and a frequency misalignment $\Delta\phi$. In order to be able to compensate negative as well as positive timing offsets, the receiver window is located in the middle of the estimated CP of the received signal and the contained signal is rotated back by half of the CP length to obtain the original signal, which is denoted by the operation $\mathscr{T}^N_{\frac{N_{CP}}{2}}$. Hence, assuming that $|\Delta\tau| < \frac{N_{\mathrm{CP}}}{2}$, the signal $y[n]$ sent to the GFDM demodulator is given by

$$y[n] = \mathscr{T}^N_{\Delta\tau}\mathscr{F}_{\Delta\phi}x[n] \tag{2.16}$$

$$= \delta[n-\Delta\tau] \circledast \left(\exp(j2\pi(\tfrac{\Delta\phi n}{K}+\phi_0))x[n]\right), \tag{2.17}$$

where

$$\mathscr{T}_\tau x[n] = \delta[n-\tau] * x[n], \qquad \mathscr{T}^N_\tau x[n] = \delta[n-\tau] \circledast x[n] \tag{2.18}$$

and

$$\mathscr{F}_\phi x[n] = \exp(j2\pi\left(\tfrac{\phi n}{N}+\phi_0\right)) \cdot x[n] \tag{2.19}$$

cause a shift in time and frequency where ϕ_0 is an arbitrary constant phase offset. $\mathscr{T}^N_\tau$ causes a circular time shift of τ samples with respect to the block length N. Accordingly, the kth subcarrier and mth subsymbol is detected by

$$\hat{d}_{k,m} = \left\langle g^{\mathrm{Rx}}_{k,m}, y[n]\right\rangle \tag{2.20}$$

$$= d_{k,m}\left\langle g^{\mathrm{Rx}}_{k,m}[n], \mathscr{T}^N_{\Delta\tau}\mathscr{F}_{\Delta\phi}g_{k,m}[n]\right\rangle + I_{k,m}, \tag{2.21}$$

where

$$I_{k,m} = \sum_{\substack{k',m' \\ (k',m')\neq(k,m)}} d_{k',m'}\left\langle g^{\mathrm{Rx}}_{k,m}, \mathscr{T}^N_{\Delta\tau}\mathscr{F}_{\Delta\phi}g_{k'm'}\right\rangle + n \tag{2.22}$$

denotes interference coming from adjacent subcarriers and subsymbols. $g^{Rx}_{k,m}[n]$ is the receiver filter shifted to the specified location in time and frequency according to (2.2).

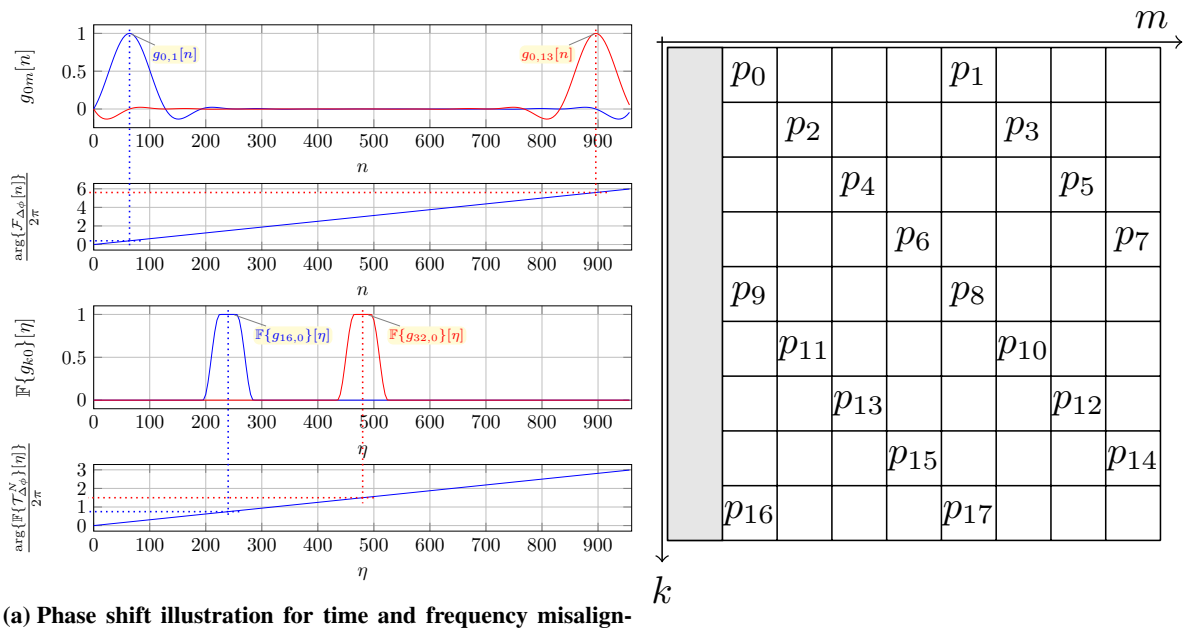

(a) Phase shift illustration for time and frequency misalignment. $M = 15$, $K = 64$, $\Delta\tau = 1$, $\Delta\phi = 0.1$

(b) Proposed piloting scheme for GFDM resouce grid.

Figure 2.6: Illustration of phase shift and piloting scheme to estimate the phase shift [MMF15].

First, let only a frequency offset appear between a user and the access point, i.e. $\Delta\tau = 0$. Looking at Fig. 2.6a we find that both $g^{\mathrm{Rx}}_{k,m}[n]$ and $g_{k,m}[n]$ are well localized in time, where the concentration is around $n = mK$. Eq. (2.19) shows, that a frequency shift actually is a multiplication of the transmit signal with a slowly rotating complex exponential. We assume the phase rotation due to this multiplication to be constant in the contributing region of $g_{k,m}[n]$ and an approximation of the phase error ϕ_m of the mth subsymbol is given by

$$\arg \hat{d}_{k,m} = \arg d_{k,m} + 2\pi\left(\tfrac{\Delta\phi m K}{K} + \phi_0\right). \tag{2.23}$$

Obviously, only the subsymbol index determines the phase error due to a frequency offset. In the frequency domain a similar chain of argumentation can be provided when no frequency offset appears but a timing offset $\Delta\tau \neq 0$. Expressing the receiver operation in the frequency domain the received data symbol is given by

$$\hat{d}_{k,m} = \mathbb{F}_N^{-1}\{G^{\mathrm{Rx}}_{k,0}[\eta] G_{k,0}[\eta] \exp(j2\pi\tfrac{\Delta\tau\eta}{N}\}|_{n=mK}, \tag{2.24}$$

where $\mathbb{F}_N\{\cdot\}$ denotes N-point discrete Fourier transform (DFT) and $G_{k,m}[\eta] = \mathbb{F}_N\{g_{k,m}[n]\}$. Due to the good frequency localization of the transmitter filter $G_{k0}[\eta]$, it is considered to be concentrated arount $\eta = kM$. By a similar argument as for the frequency offset, the phase error of the received symbols can be approximated by

$$\arg \hat{d}_{k,m} = \arg d_{k,m} + 2\pi\tfrac{\Delta\tau k M}{N} \tag{2.25}$$

for a time offset. Dual to the case of frequency-offset, the subcarrier index determines phase error when a time offset appears.

2.1.3.1 Estimation of Time and Frequency Misalignment

Naturally, when misalignments in both time and frequency occur, the phase rotation depends on both the subcarrier and subsymbol index.

Let

$$\phi_f = 2\pi\frac{\Delta\tau M}{N}, \qquad \phi_t = 2\pi\frac{\Delta\phi K}{N}, \qquad \phi_0' = 2\pi\phi_0. \tag{2.26}$$

Then, the system model used for estimation of $\Delta\phi$ and $\Delta\tau$ can be given by

$$\arg\hat{d_{k,m}} = \arg d_{k,m} + m\phi_t + k\phi_f + \phi_0'. \tag{2.27}$$

To estimate the misalignment, we introduce a piloting scheme according to Fig. 2.6b. The position of the pilots in time ($\mu(i)$) and frequency ($\kappa(i)$) is given by

$$\kappa(i) = \lfloor \tfrac{i}{2} \rfloor \tag{2.28}$$

$$\mu(i) = 1 + \left(\left(i + (i \bmod 2)\cdot\tfrac{M-1}{2}\right) \bmod (M-1)\right). \tag{2.29}$$

Using the system model (2.27) the following equation system can be stated that describes the expected phases of pilots at the receiver:

$$\arg\hat{p}_i = \arg p_i + \mu(i)\phi_t + \kappa(i)\phi_f + \phi_0'. \tag{2.30}$$

Depending on the misalignment and subcarrier and subsymbol index, $\arg p_i$ can grow larger than 2π which makes the phase rotation ambiguous. This effect is combated by not considering the absolute offset but the phase difference between adjacent pilots given by

$$\hat{\phi}_{ij} = \arg\hat{p}_i - \arg\hat{p}_j \tag{2.31}$$

$$= \underbrace{\begin{bmatrix}\mu(i)-\mu(j) & \kappa(i)-\kappa(j)\end{bmatrix}}_{\mathbf{v}_{ij}} \begin{bmatrix}\phi_t \\ \phi_f\end{bmatrix}. \tag{2.32}$$

For the present investigation we assume $\arg p_i - \arg p_j = 0$, i.e. all pilots carry the same phase information. If the estimation performance can be increased by considering different phase distributions needs to investigated in subsequent works. Now, let $\mathbf{V}$ be a matrix that contains all $\mathbf{v}_{ij}$ where the absolute value of the elements of $\mathbf{v}_{ij}$ is less or equal to $\frac{M-1}{2}$. This way, only phase differences between adjacent pilots are considered. Further, let $\mathbf{P}$ be a vector containing $\hat{\phi}_{ij}$ of the selected elements in $\mathbf{V}$. Then,

$$\mathbf{P} = \mathbf{V}\begin{bmatrix}\phi_t \\ \phi_f\end{bmatrix}. \tag{2.33}$$

Calculation of a least-squares solution

$$\begin{bmatrix}\hat{\phi}_t \\ \hat{\phi}_f\end{bmatrix} = (\mathbf{V}^H\mathbf{V})^{-1}\mathbf{V}^H\mathbf{P}. \tag{2.34}$$

provides an estimation of the phase rotations ϕ_t and ϕ_f per subsymbol and subcarrier, respectively.

2.1.3.2 Compensation of Time and Frequency Misalignment

Two possibilities arise to compensate the time and frequency misalignment: compensation in data domain and signal domain. The compensation in the data domain is simply achieved by rotating back the demodulated data symbols $\hat{d}_{k,m}$ according to the estimated phase rotation per subcarrier and subsymbols, yielding the compensated symbols $\hat{d}'_{k,m}$ given by

$$\hat{d}'_{k,m} = \hat{d}_{k,m} \cdot \exp(-j(m\hat{\phi}_t + k\hat{\phi}_f)). \tag{2.35}$$

Signal domain compensation is achieved by applying the inverse of the estimated time and frequency misalignment to the received GFDM block $y[n]$, yielding the signal $y'[n]$ given by

$$y'[n] = \mathscr{F}_{-\hat{\Delta\phi}} \mathscr{T}^N_{-\hat{\Delta\tau}} y[n], \tag{2.36}$$

where

$$\hat{\Delta\phi} = \frac{N\hat{\phi}_t}{2\pi K} \qquad \hat{\Delta\tau} = \frac{N\hat{\phi}_f}{2\pi M}. \tag{2.37}$$

Then, GFDM demodulation is again carried out, but using the compensated signal $y'[n]$. Signal domain compensation outperforms data domain compensation, because time and frequency misalignment additionally leads to inter-carrier interference (ICI) and inter-symbol interference (ISI) which cannot be compensated by the data domain compensation. However, because of the repeated GFDM demodulation, signal domain compensation requires a higher computational complexity. With the signal domain compensation, repeated iterations of compensation and estimation can be carried out to further increase the compensation performance.

2.1.3.3 Estimation and Compensation of Constant Phase Error

Once the time and frequency misalignment is compensated, only a constant phase error is left, which is compensated in a subsequent step. When $\hat{p}'_i$ and $\hat{d}'_{k,m}$ denote the pilots and data symbols after the offset compensation, the common phase error is can be estimated from the mean of the measured phase difference between known and measured pilots:

$$\hat{\phi}_0 = \overline{\arg \hat{p}_i - \arg p_i}. \tag{2.38}$$

Then, constant phase error compensation is applied on the data symbols $d'_{k,m}$, which leads to the final estimation $\hat{d}''_{k,m}$, given by

$$\hat{d}''_{k,m} = \hat{d}'_{k,m} \cdot \exp(-j\hat{\phi}_0). \tag{2.39}$$

2.1.4 Transmit Diversity Techniques with GFDM

Especially in unpredictable environments as they appear in RESCUE scenarios, it is very important to keep available links as robust as possible. The application of multi-antenna techniques which exploit spatial diversity to combat severe fading of the distinct channels between the seperate antennas can significantly help at most basic level of the PHY layer. This section describes a possibility on how space-time coding (STC) [Ala98] can be applied to GFDM to increase the robustness in a fading multipath environment by exploiting transmit diversity.

The key challenge for the application of STC to GFDM is its inherent non-orthogonality between subsymbols and subcarriers which impedes the simple approach that can be used for OFDM [LW00]. When using a linear equalizer, severe ISI is included within the estimated symbols, as shown in [MMF14b]. However, the STC can be applied to

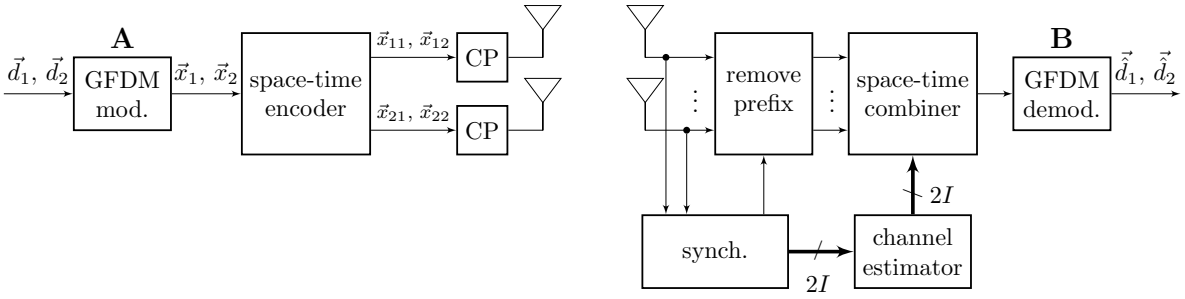

Figure 2.7: Block diagram for the proposed STC-GFDM transceiver [MMG+14b].

GFDM at a block-level instead of a symbol-level by the application of time-reversal space-time code (TR-STC). TR-STC was initially developed to provide transmit-diversity for single-carrier transmission in multipath fading environments [AlD01]. The application of TR-STC to GFDM is presented in the block diagram in Fig. 2.7. For TR-STC GFDM, two subsequent GFDM blocks $\vec{d}_1$ and $\vec{d}_2$ are independently modulated leading to

$$\vec{x}_1 = \mathbf{A}\vec{d}_1 \quad \text{and} \quad \vec{x}_2 = \mathbf{A}\vec{d}_2. \tag{2.40}$$

Then, the two subsequent blocks are processed by the space-time encoder which outputs the signals to transmit to the antenna which are given by the transformation in Tab. 2.1.

Table 2.1: Space-Time encoded GFDM signals.

	Antenna 1	**Antenna 2**
Time frame 1	$x_{11}[n] = x_1[n]$	$x_{21}[n] = -x_2^*[-n \mod N]$
Time frame 2	$x_{12}[n] = x_2[n]$	$x_{22}[n] = x_1^*[-n \mod N]$

Hence, the space-time encoder produces a time-reversed and conjugated version for the second antenna. Then, a CP is prepended to each block before signal transmission. Then, the signal of block 1 and 2 received at the ith receiving antenna after being sent through two independent wireless channels is given by

$$\begin{aligned} \vec{y}_{i1} &= \mathbf{H}_{1i}\vec{x}_{11} + \mathbf{H}_{2i}\vec{x}_{21} + \vec{w}_{i1} \\ \vec{y}_{i2} &= \mathbf{H}_{1i}\vec{x}_{12} + \mathbf{H}_{2i}\vec{x}_{22} + \vec{w}_{i2}, \end{aligned} \tag{2.41}$$

There, $\mathbf{H}_{ji}$ denotes the circulant channel matrix that represents the circular convolution of the signal with the channel between the jth transmitting and ith receiving antenna. $\vec{w}_{i1}$ and $\vec{w}_{i2}$ denote the noise vectors on the ith receiving antenna collected in the first and second frame slot, respectively. At the receiver, the space-time combining including a maximum ratio combiner (MRC) is carried out in the frequency domain given by

$$\hat{\vec{X}}_1 = \frac{\sum_{i=1}^{I} \phi_{1i}^* \vec{Y}_{i1} + \phi_{2i} \vec{Y}_{i2}^*}{\sum_{i=1}^{I} \phi_{1i}^* \phi_{1i} + \phi_{2i}^* \phi_{2i}} = \vec{X}_1 + \frac{\sum_{i=1}^{I} \phi_{1i}^* \vec{W}_{i1} + \phi_{2i} \vec{W}_{i2}^*}{\sum_{i=1}^{I} \phi_{1i}^* \phi_{1i} + \phi_{2i}^* \phi_{2i}} = \vec{X}_1 + \vec{W}_{eq_1} \tag{2.42}$$

$$\hat{\vec{X}}_2 = \frac{\sum_{i=1}^{I} \phi_{1i}^* \vec{Y}_{i2} - \phi_{2i} \vec{Y}_{i1}^*}{\sum_{i=1}^{I} \phi_{1i}^* \phi_{1i} + \phi_{2i}^* \phi_{2i}} = \vec{X}_2 + \frac{\sum_{i=1}^{I} \phi_{1i}^* \vec{W}_{i2} - \phi_{2i} \vec{W}_{i1}^*}{\sum_{i=1}^{I} \phi_{1i}^* \phi_{1i} + \phi_{2i}^* \phi_{2i}} = \vec{X}_2 + \vec{W}_{eq_2} \tag{2.43}$$

Here, I is the number of receiving antennas, $\phi_{ji} = \mathbf{F}\mathbf{H}_{ji}\mathbf{F}^{-1}$ and $\vec{Y}_{i1}$ and $\vec{Y}_{i2}$ are the DFT of $\vec{y}_{i1}$ and $\vec{y}_{i2}$, respectively. Finally, the GFDM demodulation is carried out on the time-domain signal given by

$$\hat{\vec{d}}_j = \mathbf{B}\mathbf{F}^{-1}\hat{\vec{X}}_j. \tag{2.44}$$

2.1.5 Multiple Access with GFDM

This section deals with the application of MA schemes to GFDM, leading to GFDMA. In RESCUE, perfect synchronization cannot be achieved and hence the MA scheme must be robust against timing and frequency misalignment between users. In particular, in this section we focus on the application of frequency-division multiple

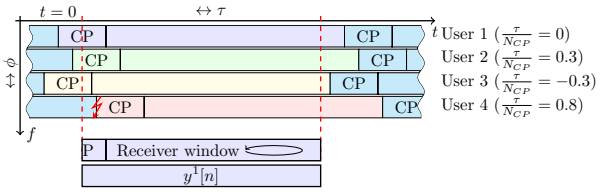

Figure 2.8: Position of the receiver window for user 1. Other users have different timing offsets [MMF15].

access (FDMA) and CSMA/CA to GFDM [MMF15], and describe the effects when timing misalignment between users occur. Especially, inter-user-interference (IUI) appears in non-synchronized MA that needs to be handled by the system. Note that in Sec. 2.1.3 methods have been described to cope with time and frequency misalignment between transmitter and receiver.

2.1.5.1 Characterization of inter-user-interference

We denote the GFDM block of the uth user by $x^{(u)}_{\text{sync}}[n]$ given by

$$x^{(u)}_{\text{sync}}[n] = \sum_{m\in\mathscr{M}} \sum_{k\in\mathscr{K}^{(u)}} d^{(u)}_{k,m} g_{k,m}[n] \quad n = 0\ldots,N-1. \tag{2.45}$$

The set of allocated subcarriers for user u is denoted by $\mathscr{K}^{(u)}$. Furthermore, adding a CP to $x^{(u)}_{\text{sync}}[n]$ yields the signal $\tilde{x}^{(u)}[n]$. Assuming each user has a time offset of $\tau^{(u)}$ time samples and a frequency offset $\phi^{(u)}$ frequency samples, the transmit signal $x^{(u)}[n]$ is given by

$$x^{(u)}[n] = \mathscr{T}_{\tau^{(u)}} \mathscr{F}_{\phi^{(u)}} \tilde{x}^{(u)}_{\text{sync}}[n]. \tag{2.46}$$

To analyze IUI, the signal is transmitted over a MA AWGN channel. At the receiver, the signals of all users add up to the signal $y[n]$ given by

$$y[n] = \sum_{u\in\mathscr{U}} x^{(u)}[n] + w[n], \tag{2.47}$$

where, $w[n]$ is AWGN at the receiver and $\mathscr{U}$ denotes the set of transmitting users. Assuming ZF receiver and perfect synchronization between transmitter and receiver, the demodulated data symbols of the uth user are given by

$$d^{(u)}_{k,m} = d_{k,m} + \underbrace{\sum_{u'\in\mathscr{U}\setminus u} \sum_{m'} \sum_{k'\in\mathscr{K}} d^{(u')}_{k'm'} \left\langle g^{Rx}_{k,m}, \mathscr{T}_{\tau^{(u')}} \mathscr{F}_{\phi^{(u')}} g_{k'm'} \right\rangle}_{I_{k,m}}, \tag{2.48}$$

where $I_{k,m}$ denotes the interference from other users onto the (k,m)th data symbol of the user of interest.

2.1.5.2 Considered Scenario

For the investigation of IUI we consider a multi-user uplink scenario that is derived from the OFDM PHY of IEEE 802.11a. In this scenario we compare the IUI when using OFDM and GFDM. In the scenario, the available bandwidth is divided into 64 subcarriers, but only 52 are allocated. The allocated subcarries are separated into 13 subchannels, where each subchannel consists of 3 subcarriers. Between subchannels, one guard carrier is inserted. This scenario is illustrated in Fig. 2.9, where also the OOB radiation of GFDM and OFDM is compared. Obviously, with GFDM a signifantly lower OOB radiation is obtained. In RESCUE, we assume that several devices are concurrently accessing the channel. Each device can choose between the available subchannels to transmit the required packet. Within each subchannel, the nodes can obey a CSMA/CA behaviour, which shows that GFDM

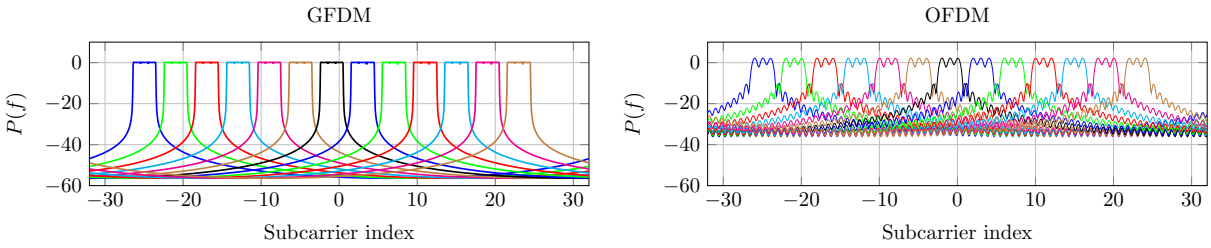

Figure 2.9: Subchannel division for the presented scenario. Subchannels are described by varying colors [MMF15].

Table 2.2: Parameters for GFDM and OFDM for performance evaluation.

Parameter	Symbol	GFDM	OFDM
# subsymbols per block	M	9	1
Allocated subsymbols	$\mathscr{M}$	$\{1,\ldots,13\}$	$\{0\}$
# available subcarriers	K	64	64
CP duration	N_{CP}	16	16
Filter	$g[n]$	RC, $\alpha = 0.1$	rect
Modulation		16QAM	16QAM

can work with acCSMA/CA as OFDM can. With this MA approach, several users can simultaneously access the channel, however, they do not overlap and can hence be easily decoupled by the destination. How to cope with collisions in CSMA/CA when using GFDM is out of scope of this Deliverable and needs to be assessed in later studies. Due to the CSMA/CA behaviour, transmissions in several subchannels is completely asynchronous. Within this scenario, we analyze the suitability of GFDM and OFDM for the PHY of the RESCUE system.

2.1.5.3 Performance Evaluation of inter-user-interference

We consider the GFDM and OFDM parameters shown in Tab. 2.2 for the subsequent evaluation. User 1 is continuously accessing subchannel 1 and user 2 is transmitting in the 2nd subchannel with varying time and frequency misalignment. This scenario is illustrated in Fig. 2.10. As a performance measure we consider the MSE of the constellation points of user 1, when user 2 is transmitting with different misalignments. The MSE is given by

$$\mathrm{MSE}(1) = E\left[\frac{1}{|\mathscr{K}^{(1)}||\mathscr{M}|}\sum_{k\in\mathscr{K}^{(1)}}\sum_{m\in\mathscr{M}}|\hat{d}_k[m]-d_k[m]|^2\right]. \tag{2.49}$$

The resulting system performance describing the MSE of user 1 is shown in Fig. 2.11, where Fig. 2.11a and Fig. 2.11b show the interference for varying time and frequency offsets, respectively. The interference on user 1 is a result of spectral leakage from user 2 into the subchannel of user 1. Therefore, GFDM can significantly outperform OFDM in this scenario.

OFDM is orthogonal when perfect frequency synchronization appears ($\phi^{(2)} = 0$), and when the timing offset is within the guard interval defined by the CP. Then, the MSE remains at the noise level of -40dB. This behaviour is illustrated by user 2 and user 3 in Fig. 2.8. As soon as $\tau^{(2)}$ grows beyond the CP length, the receiver window covers two subsequent data blocks if the interfering user. Then, orthogonality is destroyed and the constellation MSE significantly increases. This timing situation is described by User 4 in Fig. 2.8. Already with a small frequency offset ($\phi^{(2)} \neq 0$) in OFDM, the high sidelobes of the rectangular OFDM filter strongly interfere with user 1 and there is strong interference, even when the timing offset is within the timing offset. The interference appears for both positive and negative frequency offset, because the sidelobes of OFDM decay very slowly. Naturally, with a frequency offset of exactly one subcarrier, OFDM becomes orthogonal again.

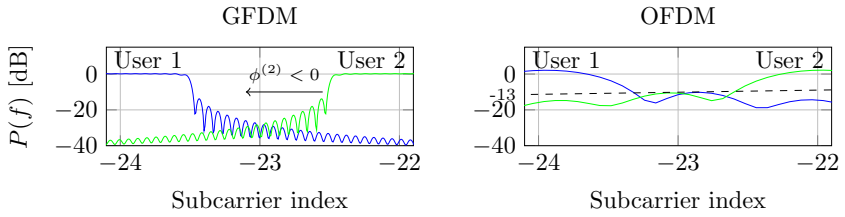

Figure 2.10: Overlapping OFDM and GFDM spectrum. OFDM does not have zeros at the subcarrier positions due to the insertion of the CP [MMF15].

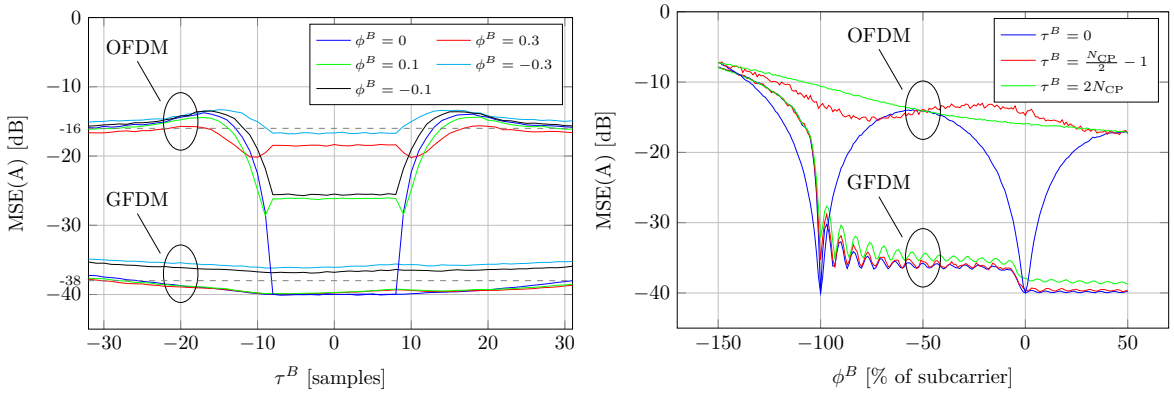

(a) Constant frequency offsets of user 2. **(b) Constant timing offsets of user 2.**

Figure 2.11: Constellation MSE for different offsets of user 2 with a noise level of -40dB and -10dB [MMF15].

The behaviour with GFDM is different. When the timing misalignment stays within the guard period and $\phi^{(2)} = 0$ the ZF receiver obtains bi-orthogonality. Accordingly, the constellation MSE remains at the noise level. As soon as the time offset increases beyond the guard interval, the same situation as in OFDM appears: (bi-)orthogonality is lost and the spectral leakage of user 2 interferes with user 1. However, because GFDM provides significanly lower sidelobes than OFDM, the MSE does only marginally increase. Even with a very small frequency misalignment $\phi^{(2)} \neq 0$, (bi-)orthogonality is also lost in GFDM. However, the MSE again only slightly increases because of the low sidelobes. Furthermore, in contrast to OFDM interferences only increases, when $\phi^{(2)} < 0$, i.e. user 2 gets closer to user 1 because the sidelobes in GFDM decay much faster than these of OFDM.

The evaluations in this section have been carried out with perfect channel state information (CSI) and known time and frequency misalignment. In real applications, the algorithms for coarse and fine synchronization described in Sec. 2.1.2 and Sec. 2.1.3 can be applied per user. Channel estimation for multi-user scenarios needs to be investigated in ongoing studies.

2.1.6 Performance analysis

This section is dedicated to summarize simulation results carried out for GFDM. First, we present the uncoded symbol error rate (SER) of the ZF GFDM receiver in various channels. Furthermore, the performance of the channel estimation algorithm presented in Sec. 2.1.3 is shown and the OOB radiation of GFDM is measured. Throughout this section, the GFDM system is configured with the paremeters listed in Tab. 2.3. The channel model we assume is derived from the WINNER model B1 “Urban micro-cell” with no LOS component [Kyö07]. The according power delay profile is given in Tab. 2.4.

In AWGN channel, compared to an orthogonal system, the noise enhancement factor (NEF) ξ determines the SNR reduction when using the ZF receiver. It is defined as

$$\xi = \sum_{n=0}^{MK-1} \left| [\mathbf{B}_{\mathrm{ZF}}]_{k,n} \right|^2, \tag{2.50}$$

Table 2.3: GFDM parameters used for simulation.

Parameter	Value
Mapping	16-QAM
Transmit Filter	RC
Roll-off (α)	0.1 or 0.9
Number of subcarriers (K)	64
Number of subsymbols (M)	9
CP length (N_{CP})	16 samples
CS length (N_{CS})	0 samples
Sampling Frequency	20Mhz

Table 2.4: Considered power delay profile of the multipath channel. Adapted from [Kyö07].

Delay (ns)	0	100	250	300	400	450	500	600
Tap Power (dB)	-1	2.9	-5.7	-12.9	-19.6	-19.8	-21.3	-26.4

which is equal for every k and depends on the employed receiver filter. For frequency-selective channels, the NEF varies for each subcarrier, but in average it is equal to ξ. A more exact equation for the NEF and the ZF SER performance in various channels is provided in [MMG+14b]. Closed-form solutions for the SER performance in AWGN-channels with a MF receiver are available in [MMG+14a].

1) *AWGN Channel*: The NEF of the GFDM system shifts the equivalent SNR. Hence, the GFDM and OFDM performance only differ by the SNR shift caused by the NEF. With the GFDM configuration from Tab. 2.3, the NEF equals $\xi = 0.05$ dB and hence GFDM and OFDM performance differ only marginally. Significantly more influence has the effect of the energy spent for insertion of the CP, which happens to be disvantageous for OFDM. The benefit in terms of spectral efficiency when comparing GFDM and OFDM is given by

$$\eta = 10\log\left[\frac{M(K+N_{\mathrm{CP}}+N_{\mathrm{CS}})}{MK+N_{\mathrm{CP}}+N_{\mathrm{CS}}}\right] \quad \mathrm{dB}. \tag{2.51}$$

Fig. 2.12(a) shown simulated and analytic results for the SER of GFDM and OFDM in an AWGN channel. As expected, GFDM can reach a lower bit error rate (BER) than OFDM because of the more efficient use of the CP.

2) *Frequency-selective channel*: In frequency-selective channels, the same behaviour as in the AWGN case is visible. OFDM and GFDM both achieve roughly the same performance, however GFDM again benifts from CP usage. For the simulation in Fig. 2.12, the channel delay profile from Tab. 2.4 has been used, where a static power delay profile was assumed.

3) *Time-variant channel*: To produce a time-variant channel the power delay profile from Tab. 2.4 was used again, however each tap is multiplied by a random variable with complex normal distribution with unit variance, which leads to a Rayleigh fading channel. It has been assumed that the channel remains constant for the transmission of one GFDM or OFDM symbol. Hence, the instantaneous SNR and SER are both random variables and therefore the average SER is plotted vs the average SNR. Fig. 2.12(c) shows the simulated results comparing OFDM and GFDM. As before in the static FSC case, GFDM outperforms OFDM due to its more efficient use of the CP. However, the difference becomes marginal due to the wide SNR range that is considered for simulations in Rayleigh fading.

4) *Space-Time Coding*: Fig. 2.13a compares the SER performance of classical STC-OFDM [LW00] with the described STC-GFDM system considering the system parameters from Tab. 2.3. As the channel the same fading model as in 3) is assumed. Note that the transmission power of the system is constant, i.e. each transmit antenna transmits with half power compared to the single-input single-output (SISO) case. The figure reveals that STC-GFDM and STC-OFDM present the same diversity gain, however GFDM outperforms OFDM because of the usage of the CP. There is a significant performance gain visible when applying space-time coding compared to the conventional SISO case.

Fig. 2.13b shows the performance of the proposed misalignment estimation and compensation algorithms from

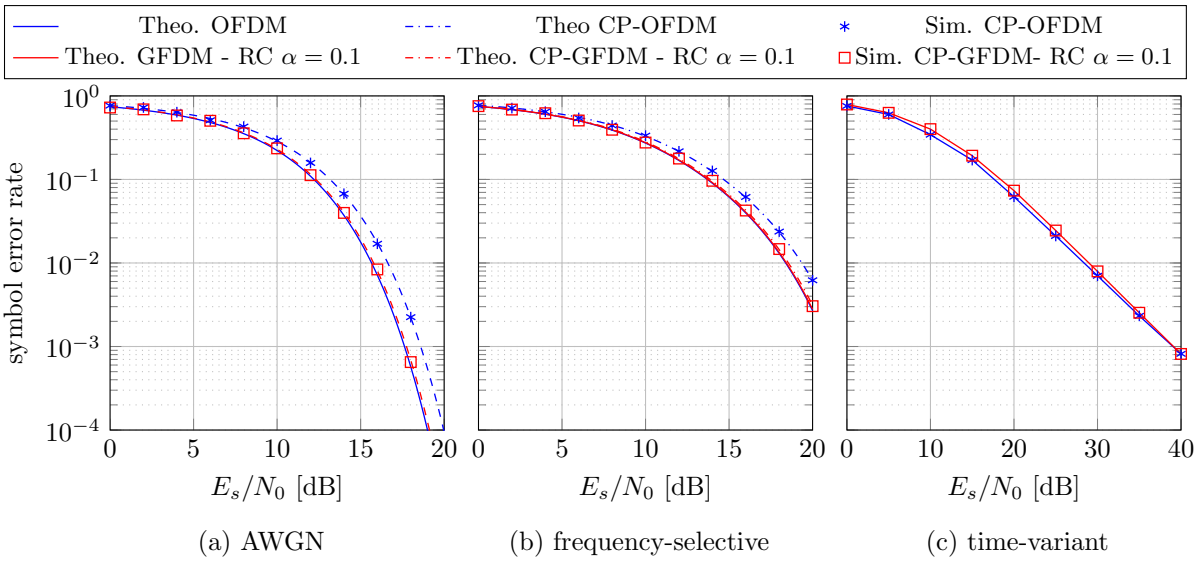

Figure 2.12: GFDM and OFDM SER performance in different channels.

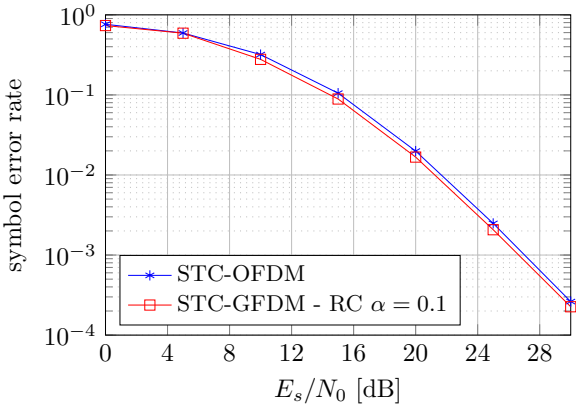

(a) SER performance of the 2x1 space-time coded systems under fading FSC.

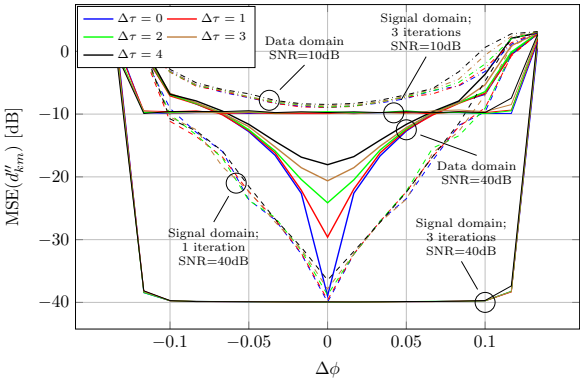

(b) Performance of misalignment compensation [MMF15].

Figure 2.13: Performance simulation for STC-GFDM and Misalignment Compensation.

Sec. 2.1.3. As a performance measure the constellation MSE of the demodulated data symbols is considered. The figure shows the compensation performance when transmitter and receiver are offset in time by $\Delta\tau$ samples and in frequency by $\Delta\Phi$ samples. The noise floor was set to -40dB and -10dB and simulations were carried out.

Obviously, the compensation in the signal domain outperforms the compensation in the data domain with one iteration. This is due to additional ISI and ICI that is generated by misalignments and which is not considered by compensation in the data domain. With one signal domain iteration, the timing misalignment can already be correctly compensated. The frequency misalignment needs more iterations and hence the MSE can be lowered by several compensation iterations. With 3 iterations, the MSE can be lowered to the noise floor for both low and high SNR. As soon as the frequency misalignment grows beyond 12% of the subcarrier bandwidth, there is an abrupt performance degradation of the compensation algorithm. In this case, the phase difference between two adjacent pilots on the same subcarrier approaches π and hence the rotation becomes ambiguous and estimation performance degrades. The performance be be increased by using different piloting structures or pilot angles within the pilot grid.

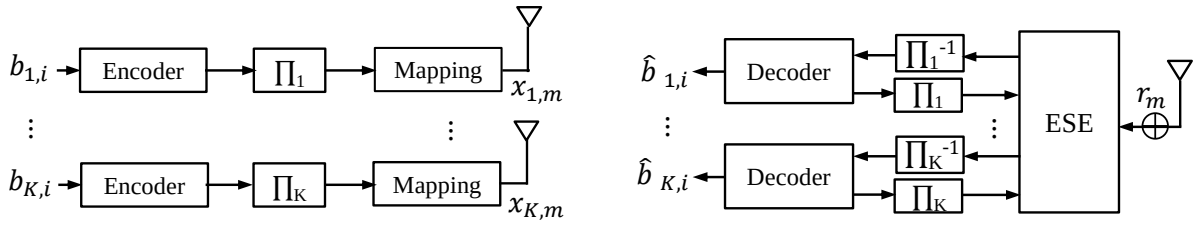

(a) The transmitter part. **(b) The receiver part.**

Figure 2.14: The system model of conventional IDMA.

2.2 Interleaved Division Multiple Access

In disaster scenarios assumed in RESCUE project where transmission links may become lossy, the forwarding nodes in the wireless sensor network may not be able to fully decode the original data sequences. However, with our proposed technique, the recovered data sequences, which may contain some errors, are allowed to be forwarded to the next node. Therefore, at the final destination node, the receiver may receive signals via many different pathes in order to enhance the detection of the original information sequence. Signals with regard to one information sequence will probably arrive at the same time, which can be formulated as a multiple access channel. In this section, IDMA is selected as our multiple access scheme, and its principles and performances are presented in the following discussion.

2.2.1 Introduction to IDMA

Nowadays, non-orthogonal multiple access (NOMA) has attracted more attention with the aim of contributing to the next generation broadband wireless communication systems, since it outperforms the orthogonal signaling technique in term of spectral efficiency[WXL06]. As one of the NOMA-based multiple access techniques, the idea of IDMA is originally inspired by Viterbi in [Vit79], and proposed in [FOO00]. After that, the IDMA concept was reformulated and introduced in [SH04; HS06] and [LLW+06]. Instead of adopting user-specific spreading sequence for user separation in code-division multiple access (CDMA) systems, IDMA employs interleavers to separate different users. Moreover, it combines iterative joint detection and channel decoding to distinguish different users according to the turbo principle. Since IDMA has a variety of design flexibility and exhibits high performance superiority, it has been proposed for many applications and considered as one the most promising candidates for future uplink wireless communications.

The system model of the conventional IDMA is shown in Fig. 2.14, where the transmitter and the receiver parts are illustrated separately. Fig. 2.14a shows the transmitter structure of the multiple access scheme under consideration of K simultaneous users. The input data $b_{k,i}$ (i denotes the time index of the users' original bit sequence) of the k-th user is encoded by forward error correction (FEC) encoder, bit-interleaved by random interleaver, and then the coded bit sequence is modulated by a specific mapping rule so that each segment of the sequence is mapped to the symbol $x_{k,m}$ (m denotes the time index of the symbol sequence). After that, the modulated signals are transmitted through mutiple access channel.

At the receiver side, as shown in Fig. 2.14b, the received signal r_m is a mixture of all the users' transmitted signals plus noise components, which can be expressed as

$$r_m = \sum_{k=1}^{K} x_{k,m} + n_m, \tag{2.52}$$

where n_m denotes the AWGN component with variance σ_n^2. However, if only information sequences of the k-th user is wanted, the interferences composed of the other users' signals can also be seen as a part of noises. Therefore, the received signal (2.52) can be rewritten as

$$r_m = x_{k,m} + \zeta_{k,m} \tag{2.53}$$

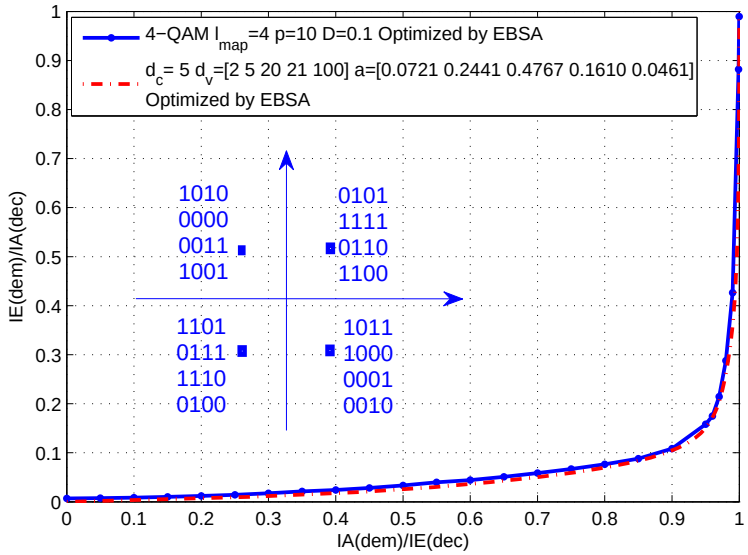

Figure 2.15: EXIT chart obtained as the result of EBSA at $SINR = -8.69$ dB (Code rate $R_c = 0.0424$, Spectrum efficiency $\eta_{\text{SPC-IrR}} = 0.1611$ bits/4QAM-symbol).

with

$$\zeta_{k,m} = \sum_{g=1,g\neq k}^{K} x_{g,m} + n_m, \tag{2.54}$$

where $\zeta_{k,m}$ indicates the multiple multiple access interference (MAI) from the other users plus AWGN It is assumed that $\zeta_{k,m}$ in (2.53) can be approximated by a Gaussian random variable. The information exchange between elementary signal estimator (ESE) and the each decoder is performed iteratively following the turbo concept.

In IDMA, the key principle is that the interleavers π_k should be different for each user. The interleavers are designed randomly and independently so that the interleaved simultaneous transmitted sequences are statistically independent. The bandwidth expansion is fully exploited for FEC coding that typically uses very low rate code, unlike in the CDMA systems. Based on the bit-interleaved coded modulation with iterative detection (BICM-ID) system design, an idea of applying BICM-ID structure into IDMA system is arisen in [WAM14], where it is found that the BICM-ID technique [FOT+12] is very suitable for designing very low rate code achieving near-capacity performance. In the technique proposed in [FOT+12], the single parity check and irregular repetition (SPC-IrR) code parameters, the doped accumulator (DACC), the modulation mixing (MM) ratio, and the labeling patterns for extended mapping (EM) are optimized in a systematic way by using the EXIT-constrained binary switching algorithm (EBSA) technique in the AWGN channel. EBSA optimizes SPC-IrR BICM-ID transmission chain that achieves close matching between the decoder and demapper's extrinisic information transfer chart (EXIT) curves even in a very low SNR range. The use of the optimized SPC-IrR BICM-ID in IDMA systems has already been investigated in [WAM14], where the excellent performance can be demonstrated via the convergence and rate region analyses. In the following sections of this chapter, the system design of the proposed BICM-ID-based IDMA, including the single-user detection (SUD) and multi-user detection (MUD) techniques, is presented, together with the performance evaluation as well as the impact analysis of power allocation on convergence and rate region characteristics.

The motivation of using very low rate SPC-IrR codes for BICM-ID based IDMA with EM has been presented in D2.1.1 in detail, from the viewpoint of the *shape* matching of their EXIT curves. Fig. 2.15 shows the result of labeling pattern optimization for 2-bit extended 4-QAM with its demapper's EXIT curve and the SPC-IrR decoder's EXIT curve; the labeling pattern and the code parameters were jointly optimized for spectrum efficiency $\eta_{\text{SPC-IrR}}$ of 0.1688 bits per 4-QAM symbol (code rate $R_c = 0.0424$) by using EBSA. The parameters related to SPC-IrR, DACC, and MM are presented in the box in the figure.

With EM, l_{map} bits are mapped on to a constellation point in the modulation part. If, 4-QAM, $l_{map} > 2$, more than

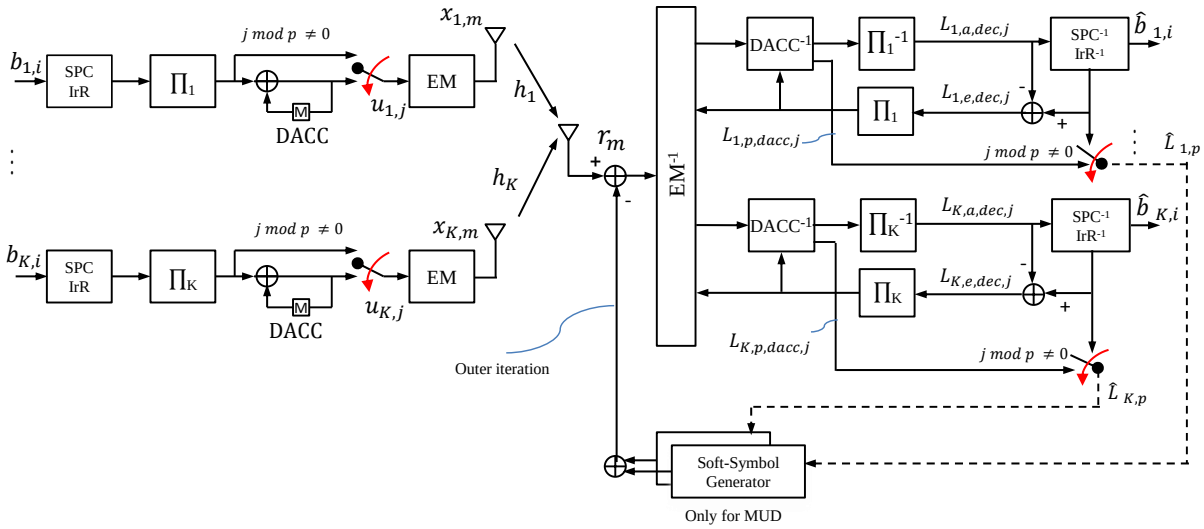

Figure 2.16: System model of the proposed BICM-ID-based IDMA system [WAM14].

one labels having different bit patterns are mapped on to each constellation point. D is the parameter that specifies the switching ratio for DACC, where every pth of the systematic bits is replaced by the accumulated coded bit [AM11]. single-parity check (SPC) code has its parameter d_c, indicating that a single parity bit is added to every $d_c - 1$ information bits. In IrR code, the parameter d_v determines the repetition times for the SPC coded bits, and the ratio is specified by parameter a.

It is found that their EXIT curves are very closely matched, however, the convergence tunnel is open until a point very close to the (1.0, 1.0) mutual information (MI) point. This result has motivated us to design BICM-ID based IDMA using very low-rate SPC-IrR.

2.2.2 Detection Schemes

The BICM-ID-based IDMA system design best utilizes the properties of BICM-ID scheme, a serial concatenation of channel coding and mapping, which requires low rate and near-capacity achieving codes. Since the performance of BICM-ID strongly depends on the matching degree between the constellation labeling pattern and the code structure, the code and mapping rule optimization technique described in the previous section provides an optimal solution to the system design. With the superiorities of the EBSA technique, the joint optimizations on codes and mapping of BICM-ID are feasible so that the designed BICM-ID scheme is well suited for applying to the IDMA system, which allocates the full bandwidth for channel coding.

The system model of the BICM-ID-based IDMA is depicted in Fig. 2.16. At the receiver side, the iterative processing between the demapper and decoder is invoked user-by-user. It has to be noted that there are two types of iterations between demappers and decoders: inner iteration and outer iteration. The inner iteration is conducted independently for each user, while the outer iteration is performed between different users. When the outer iteration is not involved in other users' signal detection, the system performs SUD; on the contrary, in MUD, the outer iteration is activated aiming to cancel the interference from the other users. Each user uses the same BICM-ID transmission structure, where the binary bit information $b_{k,i}$ of user-k, $k \in \{1, \cdots, K\}$, at the timing index i is SPC-IrR-encoded at the transmitter. The encoded bit sequence is bit-interleaved by a random interleaver Π_k, and then accumulated by DACC with the switching ratio p to generate a new bits sequence $u_{k,j}$, where j is the timing index at the output of DACC. The DACC output binary sequence $u_{k,j}$ are serial-to-parallel converted, and mapped on to a 4-QAM signal point, in part, according to the labeling pattern of EM, and in part, according to the non-Gray labeling pattern to produce transmission symbols $x_{k,m}$ at the timing index m, with modulation mixing ratio D. After that, the transmission symbols $x_{k,m}$ are transmitted to the channel. With SUD, the receiver part detects each user independently, without the any help from the other users; however, with MUD, all the simultaneous users are to be detected jointly with the help of the other users in the form of soft cancelation.

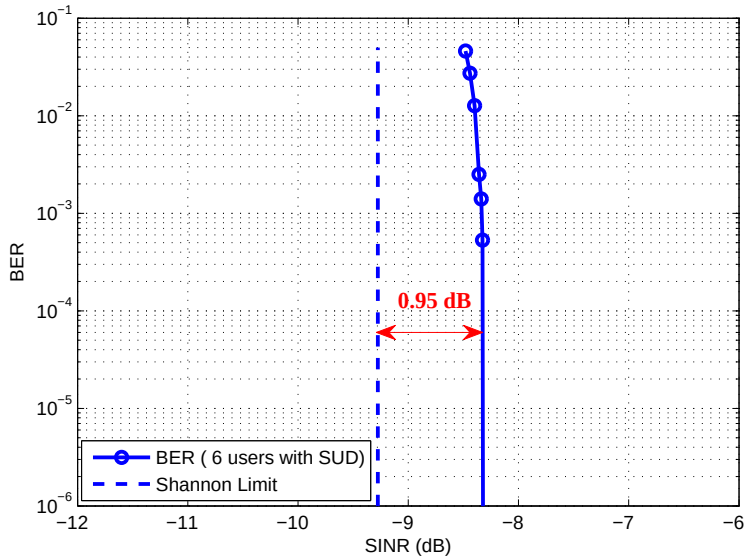

Figure 2.17: The BER peformance of IDMA-SUD with 6 users.

2.2.2.1 Single-user Detection

As described above, in IDMA systems, user separation is performed by the interleaver utilized in the iteratively decodable demapping and channel decoding system, for which its patterns have to be different user-by-user. The demapper of BICM-ID assumes that the other users are regarded as being equivalent to noise, and hence it is purely a SUD detector. Moreover, the SUD detector works together with decoder so that each user is detected independently. The detail of SUD schemes for IDMA can be found in deliverable D2.1.1.

2.2.2.1.1 EXIT Analysis of IDMA-SUD

This subsection presents results of EXIT analysis for the proposed BICM-ID-based IDMA with SUD. We exactly follow the established methods [Bri01; Hag04] when calculating the EXIT curves. SINR and SNR for each user are defined as follows

$$SINR_k = \frac{P_k}{\sum_{g=1,g\neq k}^{K} P_g + \sigma_n^2}, \tag{2.55}$$

$$SNR_k = \frac{P_k}{\sigma_n^2}, \tag{2.56}$$

where P_k, and σ_n^2 denote the power allocated to k-th user and AWGN noise variance, respectively.

Assume that the power allocated to each user is identical, i.e, $P_k = 1.0$. Fig. 2.15 shows the result of labeling pattern optimization for 2-bit extended 4-QAM ($l_{map} = 4$) with its demapper's and SPC-IrR decoder's EXIT curves; the labeling pattern and the code parameters were jointly optimized for spectrum efficiency $\eta_{\mathrm{SPC-IrR}}$ of 0.1688 bits per 4-QAM symbol (code rate $R_c = 0.0424$) by using EBSA. The parameters related to SPC-IrR, DACC, and MM are presented in the box in the figure. With this very low code rate, because of the area property, the area under the decoder curve is very small, which means that the decoder EXIT curve exhibits a "reverse-L" shape, and so is the demapper's EXIT curve. Because they are closely matched, near-capacity performance, very sharp BER threshold and error-floor removal (or reduction to a value range below $10^{-6} - 10^{-5}$ of BER) can be expected with the designed very low-rate code. Note that IDMA-SUD uses the code parameters and labeling pattern shown in Fig. 2.15.

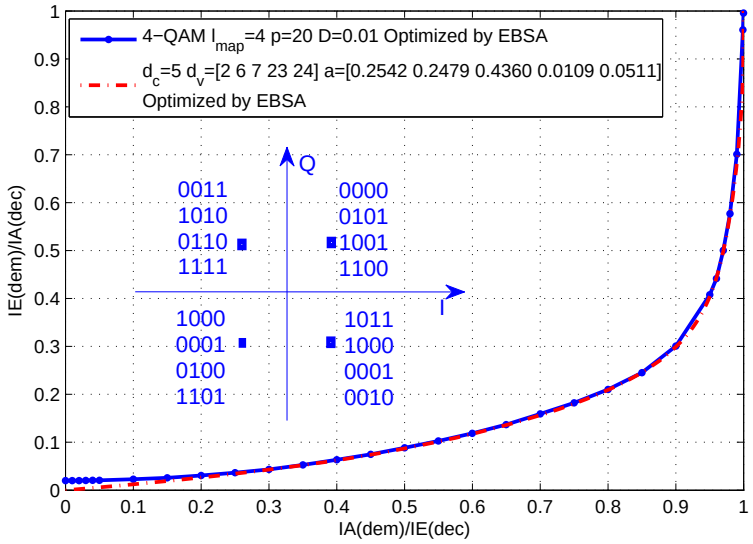

Figure 2.18: EXIT chart of IDMA-MUD technique at $SNR_k = -3.8$ dB, $k = 1,2$ (Code rate $R_c = 0.1226$, Spectrum efficiency $\eta_{SPC-IrR} = 0.4879$ bits/4QAM-symbol) [WAM14].

2.2.2.1.2 Performance Evaluation of IDMA-SUD

BICM-ID-based IDMA-SUD does not require soft interference cancellation, and it only performs demapping and decoding, user-by-user, independently, without providing any *a priori* information to help the other users. Therefore, with IDMA-SUD, the BER performance versus SINR, defined by (2.55), is not affected by the number of the users, if the total user number K and the noise variance σ_n^2 are fixed. Fig. 2.17 plots BER performance of the proposed BICM-ID-based IDMA-SUD for $K = 6$, shown by "○". The BER threshold is very sharp, and no error floor can be observed (or invisible within the BER value range shown in the figure). It is found that the threshold SINR is around -8.69 dB, which is exactly consistent with the EXIT chart shown in Fig. 2.15, and this observation is independent of the number of the simultaneous users. The consistency between Figs. 2.15 and 2.17 indicates that it is reasonable to approximate the composite signal composed of the simultaneous users' signals plus Gaussian noise by equivalent Gaussian noise having the same power, at least, in a low enough SINR range.

2.2.2.2 Multi-user Detection

In MUD, soft replica of each user's signal is subtracted from the received composite signal, of which process is referred to as soft cancellation. The outer iteration shown in Fig. 2.16 is now activated which indicates the outer iteration is included in MUD. The detection scheme for MUD is detailed in deliverable 2.1.1.

2.2.2.2.1 EXIT Analysis of IDMA-MUD

As stated before, we assume the simplest two-user (K=2) IDMA MAC scenario to identify the convergence property and to focus on the impact of unequal power allocation. We first draw the demapper's EXIT curve by assuming that all the other users' signals are cancelled and we only consider one user. This assumption is reasonable because as described above, labeling patterns and coding parameters are determined by the EBSA algorithm so that two EXIT curves are very closely matched, and hence very sharp BER threshold can be expected. This means that if the labeling patterns and coding parameters are designed at a specified SNR value, soft successive interference cancellation (SSIC) can gradually but finally completely eliminate the other users' signals, without having to involve any statistical signal processing-based interference cancellation, as opposed to [KBU09]. The EXIT curve obtained by using EBSA is presented in Fig. 2.18 for $SNR_k = -3.8$ dB. Since the simultaneous users provide the LLR feedback to each other, three-dimensional (3D) EXIT curves are used to visualize the convergence property.

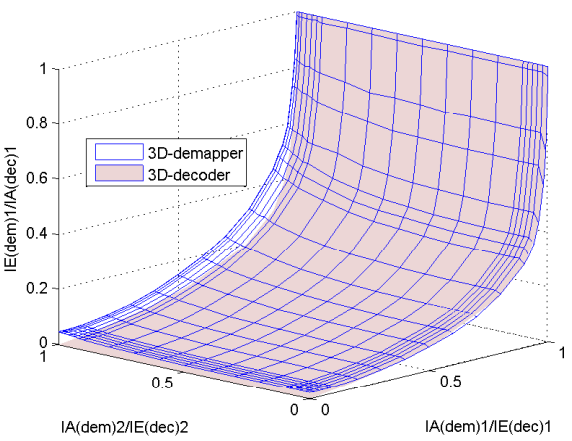

(a) Equal power allocation, $(P_1 + P_2)/\sigma_n^2 = 2.21$ **dB,** $SNR_1 = SNR_2 = -0.8$ **dB.**

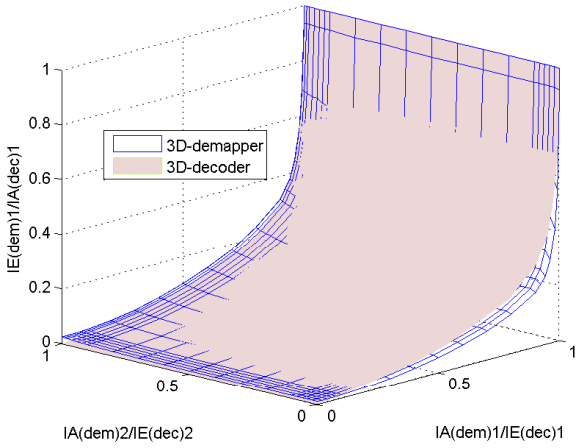

(b) Unequal power allocation, $(P_1 + P_2)/\sigma_n^2 = 0.63$ **dB,** $SNR_1 = -3.29$ **dB,** $SNR_2 = -1.62$ **dB.**

Figure 2.19: 3D EXIT chart of IDMA-MUD technique with equal and unequal power allocation [WAM14].

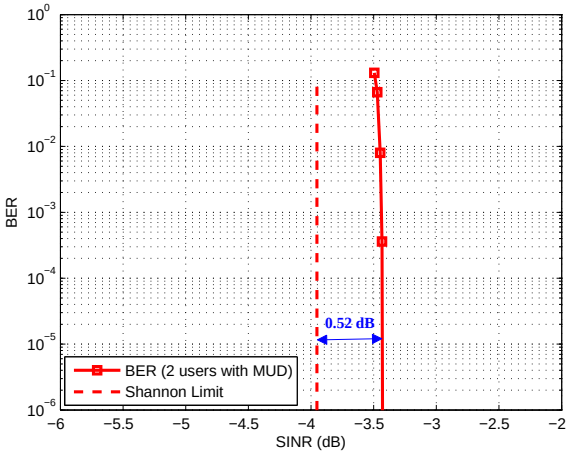

(a) The BER performance of IDMA-MUD.

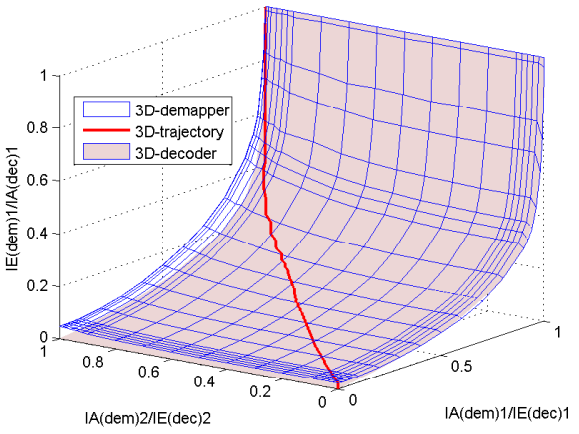

(b) The trajectory of IDMA-MUD with equal power allocation, $SNR_1 = SNR_2 = -0.8$ **dB [WAM14].**

Figure 2.20: Performance of IDMA-MUD.

2.2.2.2.2 Unequal Power Allocation

Assume that the powers allocated to different users are unequal, or, equivalently, the transmit signal per user is faded independently and hence the received power per user at the base station (BS) is different. To keep comparison fair, the total receive power P_{total} is kept constant. In this chapter, $P_{total} = 2.0$, for all the scenarios tested with two-user IDMA-MUD, and the noise variance is changed accordingly in this case. Fig. 2.19b presents the 3D EXIT chart in an unequal power allocation scenario where the ratio $P_1/P_2 = 0.68$, $SNR_1 = -3.29$ dB and $SNR_2 = -1.62$ dB. It is found that the two planes intersect at the most of the middle part where the decoder's EXIT plane is obviously above the demapper's. However, there still remains a gap, through which the trajectory is expected to go through and reach a point very close to the (1.0, 1.0, 1.0) mutual information point. It should be noticed that for the both users, the SNR value is less than -0.8 dB, which is the case of equal power allocation, tested in the equal power allocation's case described above. This makes significant impact on the MAC region to be analysed in section 2.2.3.

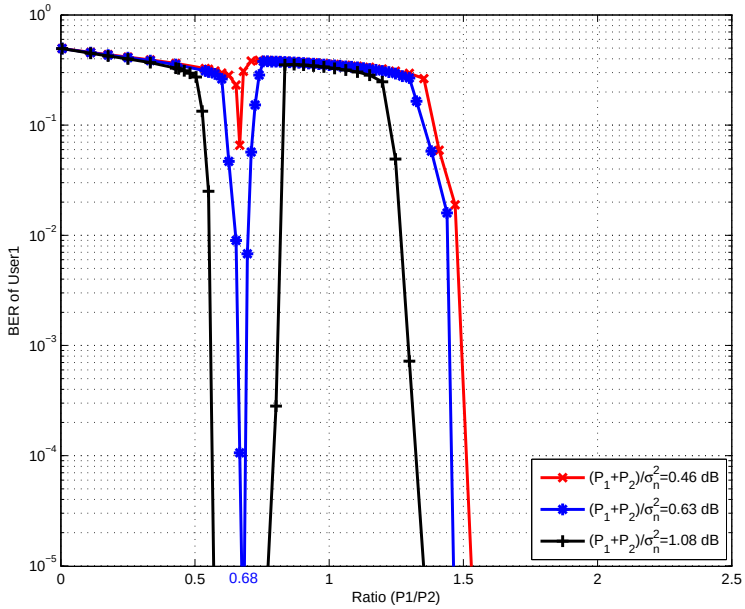

Figure 2.21: BER performance of IDMA-MUD for $K = 2$ users with unequal power allocation [WAM14].

2.2.2.2.3 Performance Evaluations of IDMA-MUD

The significant contribution of the research on BICM-ID-based IDMA over AWGN channels is the impact analysis of equal and unequal power allocation on MUD convergence property, also by using the multi-dimensional EXIT chart. Note again that since we assume only the simplest two-user IDMA in single-path AWGN channels, power allocation is intuitively equivalent in meaning to each user's transmit signal power. It is shown that with unequal power allocation, smaller total received SNR is required to achieve the BER threshold than with the equal power allocation. This result is consistent to [Ver98].

With the proposed BICM-ID-based IDMA technique, excellent BER performance versus SINR can be achieved with SUD. However, when the number of users increases, BER versus each user's SINR, defined by (2.55), degrades due to the multiple access interference from the other simultaneous users. Therefore, to achieve better performance, a technique to reduce or to ultimately eliminate the interference, such as SSIC, is needed. Again, the simplest two-user scenario is assumed, and this sub-section investigates the BER performance of user 1 with the SSIC IDMA-MUD without loss of generality. The trajectory indicating the mutual information exchange obtained through chain simulation is also presented.

2.2.2.2.4 Performance of Equal Power Allocation

Fig. 2.20b presents 3D EXIT chart and the trajectory of the proposed BICM-ID-based IDMA-MUD for $K = 2$ users, respectively, where the $SINR_1 = SINR_2 = -3.43$ dB ($SNR_1 = SNR_2 = -0.8$ dB and $(P_1 + P_2)/\sigma^2 = 2.21$ dB). The BER performance in this scenario is shown by "□" in Fig. 2.20a. With our proposed technique, the BER threshold is very sharp and no error-floor is visible in the BER range. Due to the exactly matched EXIT curves combined with the soft cancellation technique, very near-capacity performance, only 0.52 dB away from the limit, can be achieved. It is found that the trajectory directly goes through the middle part between the two planes, and reaches a point very close to the (1.0, 1.0, 1.0) mutual information point, as expected in subsection 2.2.2.2.1.

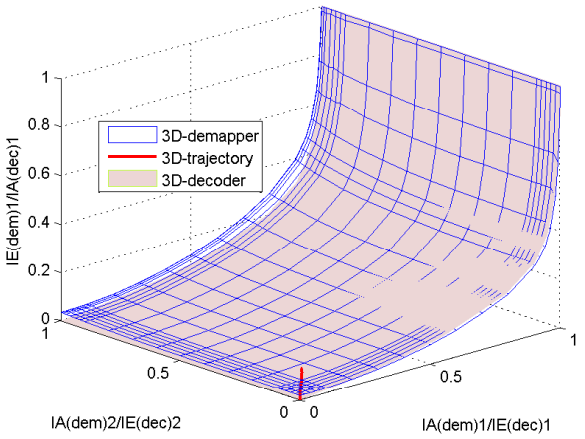

(a) $P_1/P_2 = 1$**,** $(P_1+P_2)/\sigma_n^2 = 0.63$ **dB.**

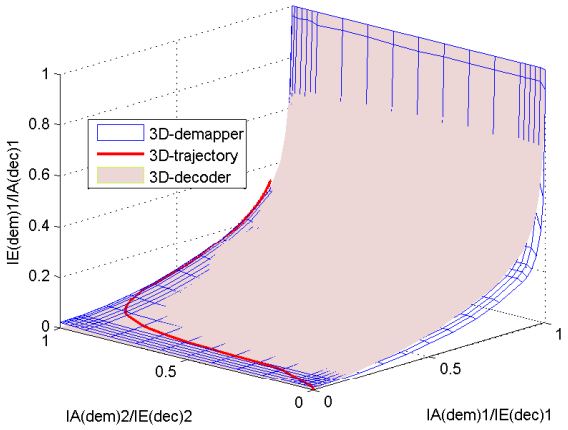

(b) $P_1/P_2 = 0.6$**,** $(P_1+P_2)/\sigma_n^2 = 0.63$ **dB.**

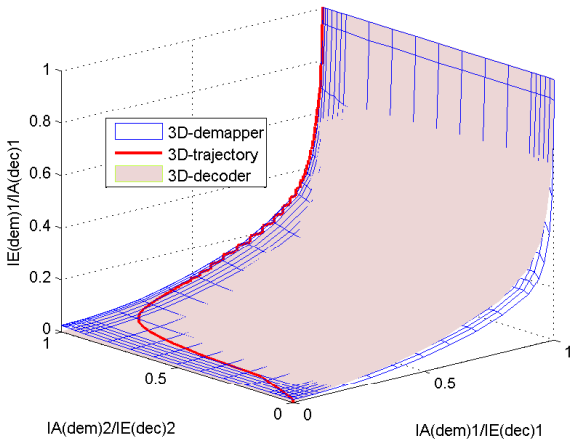

(c) $P_1/P_2 = 0.68$**,** $(P_1+P_2)/\sigma_n^2 = 0.63$ **dB.**

Figure 2.22: The trajectories of IDMA-MUD with unequal power allocation [WAM14].

2.2.2.2.5 Performance of Unequal Power Allocation

Assume that the total power is fixed as $(P_1+P_2)=2.0$ such that $(P_1+P_2)/\sigma_n^2 = 1.08$ dB, while changing the ratio of P_1/P_2. The results of the simulations conducted to evaluate the BER performance with unequal power allocation, are plotted in Fig. 2.21. It is found from the figure that the BER curve shown by "+" for user 1 first decreases very sharply as the ratio P_1/P_2 increases, and it becomes lower than 10^{-5} between $P_1/P_2 = 0.58$ and $P_1/P_2 = 0.75$, and then it suddenly increases to a value larger than 10^{-1}, when $P_1/P_2 \cong 1.0$. Then, after that, it sharply decreases again when $P_1/P_2 \geq 1.3$. When the $(P_1+P_2)/\sigma_n^2$ is decreased to 0.63 dB, the BER curve shown in "*" has almost the same tendency, still the rapid decrease in BER can be found around $P_1/P_2 = 0.68$, when the ratio $P_1/P_2 < 1.0$. However, the BER curve shown in "×" is for $(P_1+P_2)/\sigma_n^2 = 0.46$ dB where the same labeling pattern and code parameters, including the switching and mixing ratios, p and D, respectively, are used as in the case of $(P_1+P_2)/\sigma_n^2 = 1.08$ dB. A similar tendency can be observed but the rapid decrease in BER can not be observed, when the ratio $P_1/P_2 < 1.0$. Hence, $(P_1+P_2)/\sigma_n^2 = 0.63$ dB is identified as the limit case with this code parameters set and labeling pattern. In the following part, we focus on the limit case so as to make comparison among several unequal power allocation cases as well as with a counterpart technique, shown in section 2.2.3.

The trajectories representing the mutual information exchange are investigated at the ratios of $P_1/P_2 = \{1.0, 0.6, 0.68\}$ with $(P_1+P_2)/\sigma_n^2 = 0.63$ dB. Fig. 2.22a shows the trajectory for $P_1/P_2 = 1.0$ in the 3D EXIT chart. It is found that although there is a gap between the planes of demapper and decoder, the trajectory is stuck at a relatively low mutual information point. This is because with $P_1/P_2 = 1.0$, $SNR_1 = SNR_2 = -2.38$ dB and $(P_1+P_2)/\sigma_n^2 = 0.63$ dB, the two planes are so close to each other around the (0.0, 0.0, 0.0) mutual information point and hence the trajectory can not go through the tunnel. Fig. 2.22b shows the trajectory for $P_1/P_2 = 0.6$ ($SNR_1 = -3.62$ dB, $SNR_2 = -1.4$ dB and $(P_1+P_2)/\sigma_n^2 = 0.63$ dB). It is found that the two planes intersect in the most of the middle part of the 3D EXIT chart, however, there still exists a small gap on the left side, and the tunnel is open until the *extrinsic* mutual information of the demapper for user 1 is around 0.35 and hence the trajectory can reach the point (demapper's *extrinsic* mutual information = 0.35 for the *user*1). Furthermore, it is found from the trajectory that for user 2, decoder's *extrinsic* mutual information reaches very close to 1.0. This means that user 2 can be nearly fully detected without errors while user 1 can not be fully detected. Fig. 2.22c presents the trajectory for $P_1/P_2 = 0.68$ ($SNR_1 = -3.29$ dB, $SNR_2 = -1.62$ dB and $(P_1+P_2)/\sigma_n^2 = 0.63$ dB). It is found that the two planes intersect in the most of the middle part of the 3D EXIT chart, but a gap still exists near the left edge of the two planes, and the tunnel opens until a point very close to the (1.0, 1.0, 1.0) mutual information point. The trajectory can sneak through the gap between the two planes, and reach the point very close to (1.0, 1.0, 1.0) mutual information point, which also means both the two users can be fully detected, even with smaller $(P_1+P_2)/\sigma_n^2$ value (0.63 dB), compared with equal power allocation case, whose $(P_1+P_2)/\sigma_n^2$ value is 2.21 dB.

2.2.3 MAC Rate Region Analysis

It is of our great interest to make the MAC rate region comparison between equal and unequal power allocation cases, as well as between our proposed and [KBU09]'s proposed technique. The scenario with $K=2$ is considered for the both equal and unequal power allocation cases. To calculate the MAC rate region, we assume that all the users use Gaussian codebook. The points A_1 and A_2, as defined in Fig. 2.23, are given by

$$A_1 = C\left(\frac{P_1}{\sigma_n^2}\right), \tag{2.57}$$

$$A_2 = C\left(\frac{P_1}{P_2+\sigma_n^2}\right), \tag{2.58}$$

with $C(x) = \log_2(1+x)$.

B_1 and B_2 are defined in the same way as the points A_1 and A_2 by replacing the user index 1 by 2. Moreover, since we are assuming $P_1 = P_2 = 1.0$ for the case of equal power allocation, and $P_1+P_2 = 2.0$, while changing σ_n^2 and P_1/P_2 values for the unequal power allocation case.

From Fig. 2.20a we first determined the $SINR_k$ value required to achieve 10^{-6} BER for $P_1/P_2 = 1.0$ and $(P_1+P_2)/\sigma_n^2 = 2.21$ dB, then, all the values of the argument of $C(x)$, which is needed to calculate (2.57)–(2.58), can be determined for equal power allocation case. For the unequal power allocation case, those values were directly obtained from $P_1/P_2 = 0.68$, $(P_1+P_2)/\sigma_n^2 = 0.63$ dB and $P_1+P_2 = 2.0$ (recall that the rapid decrease of BER

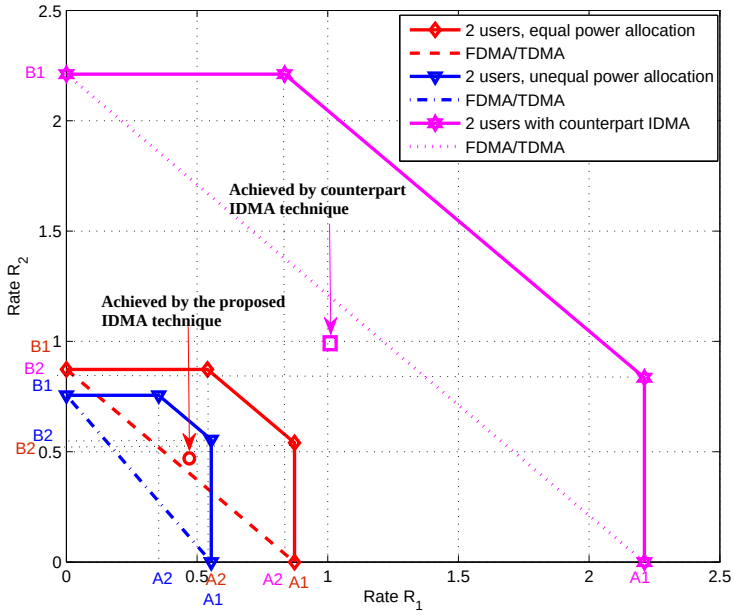

Figure 2.23: Gaussian multiple access channels for $K = 2$ users (the comparison between our proposed IDMA technique (with equal and unequal power allocation cases) and IDMA counterpart technique proposed by [KBU09]), equal power allocation: $SNR_1 = SNR_2 = -0.8$ dB, unequal power allocation: $SNR_1 = -3.29$ dB, $SNR_2 = -1.62$ dB [WAM14].

happens at $P_1/P_2 = 0.68$, as shown in Fig. 2.21). Fig. 2.23 shows the MAC rate regions (or MAC-pentagon) with the equal and unequal power allocation cases. It is found that the MAC rate region with unequal power allocation is smaller than that with equal power allocation. However, the achieved spectrum efficiency of two cases are the same, i.e, $R_1 = R_2 = \eta_{\text{SPC-IrR}} = 0.4879$ bits per 4-QAM symbol, which is shown in Fig. 2.23 by "$\circ$". This confirms that unequal power allocation can achieve the same spectrum efficiency with smaller SNR values.

The dotted line connecting A_i and B_i, $i = \{1,2\}$, corresponds to two-user orthogonal signalling such as frequency or time division multiple access (FDMA or TDMA). It is found that with both the equal and unequal power allocation cases, the rate-pair plot is above the FDMA/TDMA line, and with the unequal power allocation, the plot is closer to the theoretical MAC rate region.

The upper bound of the sum-rate $R_1 + R_2$ is given by

$$R_1 + R_2 \quad \leq \quad C\left(\frac{P_1 + P_2}{\sigma_n^2}\right) \tag{2.59}$$

It is found from Fig. 2.23 that the MAC rate region with unequal power allocation is smaller than that with equal power allocation, and obviously, with the unequal power allocation, the MAC region is not symmetric. With the equal power allocation ($SNR_1 = SNR_2 = -0.8$ dB), the sum-rate bound B_{equal} is 1.41, while with unequal power allocation ($SNR_1 = -3.29$ dB and $SNR_2 = -1.62$ dB), the sum-rate bound $B_{unequal}$ is 1.1. Therefore, we can conclude that the achieved sum-rate $R_1 + R_2 = 2 \times 0.4879$, and $R_1 + R_2 < B_{unequal}$ ($SNR_1 = -3.29$ dB and $SNR_2 = -1.62$ dB)$<B_{equal}$ ($SNR_1 = SNR_2 = -0.8$ dB). It can be concluded that to achieve the same spectrum efficiency ($\eta_{\text{SPC-IrR}} = 0.4879$), unequal power allocation requires smaller *SNRs* values for each user.

It is interesting to make comparison of the achieved rate pair and the MAC rate region between our proposed and [KBU09]'s proposed techniques. Since [KBU09] assumes an 8 user IDMA scenario, we converted the rate pair and the MAC region to the two-user case by the following method: first of all, we identified the SNR value, required to achieve 10^{-6} BER from Fig. 3 in [KBU09]. Since, in [KBU09], all users use the same code, which achieves 0.2550 bits per 4-QAM symbol, and the same power is allocated to them, A1 point in Fig. 2.23 can be calculated by assuming that 6 out of 8 users are totally cancelled, and A2 by assuming that 6 out of 8 users are equivalent to noise. The point B1 and B2 can also be calculated in the same way.

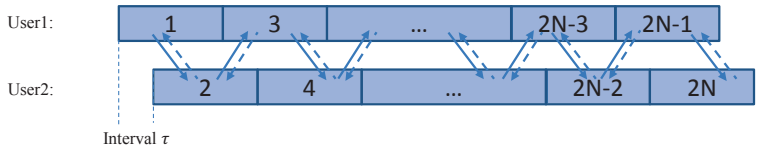

Figure 2.24: Asynchronous frame timing.

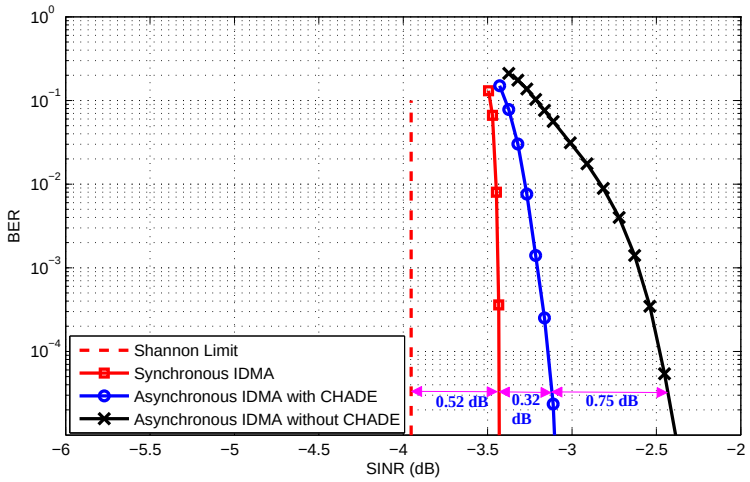

Figure 2.25: The comparison of the BER performance between synchronous and asynchronous IDMA.

Since spectrum efficiency of the system proposed in [KBU09] is 0.2550 bits per 4-QAM symbol for all the 8 users, it is equivalent to each user's spectrum efficiency of 1.02 bits per 4-QAM symbol in two-user case, assuming a Gaussian codebook. The calculated MAC region and the rate pair (indicated by "□") obtained by converting from 8 user IDMA to two-user IDMA are also shown in Fig. 2.23. It is found that surprisingly the achieved rate pair with [KBU09]'s technique is lower than the FDMA/TDMA line with a Gaussian codebook. Obviously, this is because the code used in [KBU09] (a convolutional code combined with a low rate repetition code) can achieve neither near-capacity performance nor very sharp BER threshold.

As one of the future works, the RESCUE project will include correlated source transmission in MAC channels, by analysing the combination of Slepian-Wolf and MAC rate region. In the previous contribution, the arrival time of signals containing correlated information is assumed to be different, such as in the Slepian-Wolf relay system. However, it is quite likely that the signals containing correlated information will mixed at the receiver so that multiuser detection technique has to be invoked. Consequently, new theoretical rate analysis and decoding algorithm design has to be conducted in order to provide a spectrum efficient solution. Based on the discussion above, IDMA is believed to be one of the promising techniques which could be competent at this matter.

2.2.4 Asynchronous IDMA

The scenario assumption made for the BICM-ID-based IDMA algorithm design and performance evaluation, described above, has assumed the perfect synchronism among the different users. Since IDMA uses interleavers to distinguish different users. Interleaver also plays an important role in the iterative detection. This observation indicates that IDMA detects the signals of each user by considering the other users' signals as being equivalent to noise, regardless of the relationship among the different users as in the soft cancelation process. For example, in SUD, when concentrating on one user, the other users' signals are equivalent to noise. So does in the inner iteration of MUD. Hence, it is supposed that proposed IDMA is robust against the frame-asynchronism.

In order to study this issue, we construct an asynchronous BICM-ID-based IDMA system model by adding certain transmission delay for each user. As shown in Fig. 2.24, for simplicity, we consider the case where there are 2 users in the transmitter part. However, the later on proposed algorithm can be extended in a straight-forward way

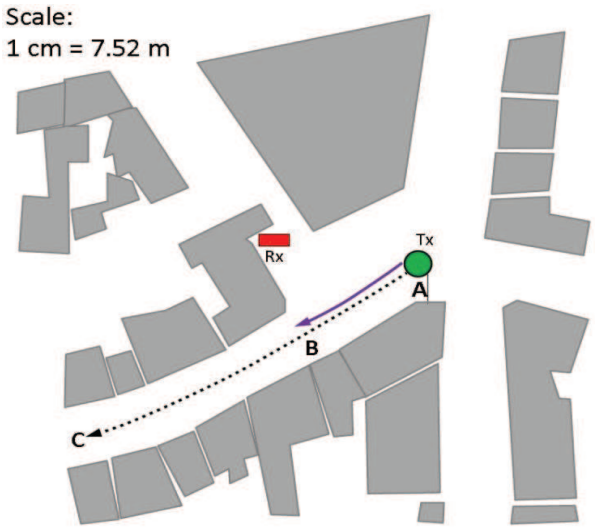

Figure 2.26: Overview of measurement route (Tx) and the position of fixed Rx [AM13].

to more users. The transmission delay, between 2 different users's transmitted siganls, is defined as the interval τ. Thus, in the receiver part, the received signal is the mixture of two asynchronous users' signals with a delay interval τ plus noise. Here, we assume that the start and end point of each frame is known.

In Fig. 2.24, since each frame of user 1 is not synchronized with each frame of user 2, for example the first frame of user 2 is overlaping with the first and second frames of user 1. Performing the MUD technique described above neither between the first frame of user 2 and the first frame of user 1 nor between the first frame of user 2 and the second frame of user 1 can fully eliminate the interference from the other user. To detect the asynchronous received frames as shown in Fig. 2.24, we propose a chained detection (CHADE) technique, with which multiple frames are jointly detected by performing the iterative MUD on the frame by frame basis with the order indicated in each frame, $1, 2, ..., 2N-1, 2N$, as shown in Fig. 2.24: start from the first frame of user 1, then the first frame of user 2, ..., until the last frame of user 1 and the last frame of user 2, as illustrated with the solid arrows. Then, soft cancelation applies to the each signal's overlapping parts. After the soft cancellation, the frame-wise detection is again performed but in backward direction, i.e. $2N, 2N-1, ..., 2, 1$, as illustrated with the dashed arrows. This forward and backward recursion is repeated until all the frames are detected.

The computer simulations are conducted to evaluate the BER performance of the constructed asynchronous IDMA system with delay interval, τ symbol-durations (τ is a random integer that uniformly distributes in the range 1 to 100). The code parameters and labeling pattern are the same as shown in Fig. 2.18 with the transmitted symbol length 20000. The simulation results are presented in Fig. 2.25, where the curve plotted with "$\circ$" is the BER performance of the asynchronous IDMA with performing the proposed CHADE technique and the curve shown with "$\times''$ is the BER performance of the asynchronous IDMA without performing the CHADE technique. It can be observed that the BER performance with CHADE technique outperforms that without CHADE technique, which indicates that with the CHADE technique, the BER performance has been improved 0.75 dB. Then, the comparison is made between the BER performance of the asynchronous IDMA with performing the proposed CHADE technique and the BER performance of the synchronous IDMA described in Fig. 2.20a. It is found that the BER performance of the asynchronous IDMA proposed with performing the proposed CHADE technique is very close to the synchronous case, only 0.32 dB gap between the two cases. This comparison shows that the proposed IDMA system is robust against the frame-asynchronism.

2.2.5 Initial Measurement Data-based Evaluation

Our proposed system is verified by using measurement data in a more practical environment. The measurement data used in this section, named "Apothekerbrunnen", was measured and recorded in the city center of Ilmenau, Germany. The geographical environment of that measurement campaign, from the top view, is shown in Fig. 2.26,

Item	Setting
Scenario name	"Apothekerbrunnen"
Scenario type and place	outdoor, city center of Ilmenau, Germany
Channel sounder	RUSK ATM
Transmit power	ca. 27 dB m at the TX switch input
Carrier frequency	5.2 GHz
Bandwidth	120 MHz
Channel impulse response length	1.6 μ_cs (number of taps 193)
Number of measured channels within one snapshot	272 (16×16 including guard interval)
Approx. snapshot distance in time	20 ms (indirect corresponding to measurement rate)
Tx array	16 elements UCA, vertical polarization only, mounted on a measurement trolley (height approx. 1.30m)
Rx array	8 elements PULA, vertical and horizontal polarization, 5.50 m above ground
Tx vehicle	hand driven trolley carrying the transmitter
Rx vehicle	fixed base station position (Receiver)

Table 2.5: Measurement campaign setup.

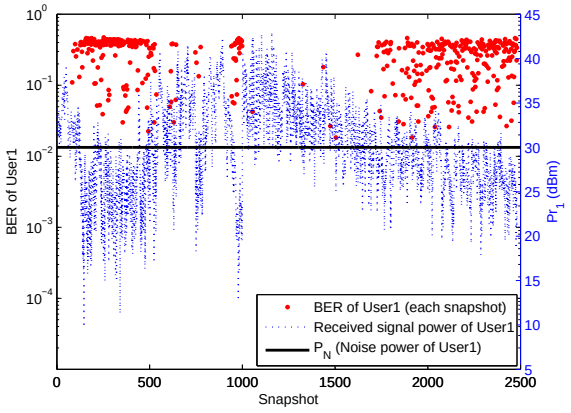

(a) BER performance with measurement data-based channels.

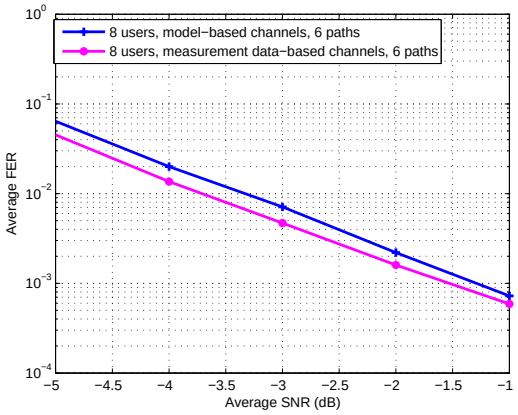

(b) Average FER performance with measurement data-based channels.

Figure 2.27: Performance of real-world measurements.

where the measurement has a length about 60 m and was sampled with 2481 snapshots, corresponding to a distance about 0.024 m between each pair of the neighboring snapshots. At the transmitter side, an 16-element uniform circular array (UCA) was used, and the transmitter was indicated by Tx. The Tx was moved along the route marked by the dashed line shown in Fig. 2.26 at walking speed. The receiver side used an 8-element uniform linear array (ULA) which is fixed in a certain position about 5.5 m above the ground, and the receiver in Fig. 2.26 is indicated by Rx.

The measurment route can roughly be divided into two regions as shown in Fig. 2.26: (1) the first part in front of the large open place, route A $\rightarrow$ B, is mainly dominated by line-of-sight line-of-sight (LOS) propagation; (2) the second part, route B $\rightarrow$ C from the open place into the pedestrian street, is non-line-of-sight non line-of-sight (NLOS) region, where the snapshot positions are surrounded by buildings with a height about 10 to 15 m. The major specifications of the measurement campaign and the antenna setup are summarized in Table. 2.5

2.2.6 Measurement Data-based Simulations and Evaluations

A series of computer simulations were conducted to verify the performance of the proposed system in realistic scenarios by using channel sounding measurement data. The system scheme we use here is exactly the same as our

design in previous sections in this chapter, where the joint turbo equalization and BICM-ID-based IDMA model was used. The code parameters and labeling pattern are optimized by EBSA with each user's $SNR_k = 0$ dB. 8 simultaneous users ($K = 8$) and 6 paths ($L = 6$) were considered in the simulations, and the sufficient outer and inner iterations were performed (10O, 20I).

- Simulation results on BER performance for each snapshot in the view point of user 1 are shown in Fig. 2.27a, where the BER performance versus the relationship between received signal power Pr_1 and noise power P_N are presented. In Fig. 2.27a, it is found that the BER performance (indicated with dots) of user 1 (each snapshot) are classified into either 0 or almost 0.5. The BERs are 0 when the received power Pr_1 (indicated with dashed curve) $>$ noise power P_N (indicated with solid line), which indicates the SNR is larger than 0 dB. On the contrary, when the received signal power $Pr_1 <$ noise power P_N, which indicates SNR is smaller than 0 dB, BERs are almost 0.5. This correponds to the EXIT chart optimized by EBSA, which further indicates the turbo cliff in BER performance happens around SNR=0 dB.

- Simulation results on average FER performance are shown in Fig. 2.27b, where the average FER performances with measurement data-based channels (indicated with "*") and with model-based channels (indicated with "+") are presented. It is observed that the consistency between measurement data-based and model-based FER performances has been proven, especially in terms of diversity order.

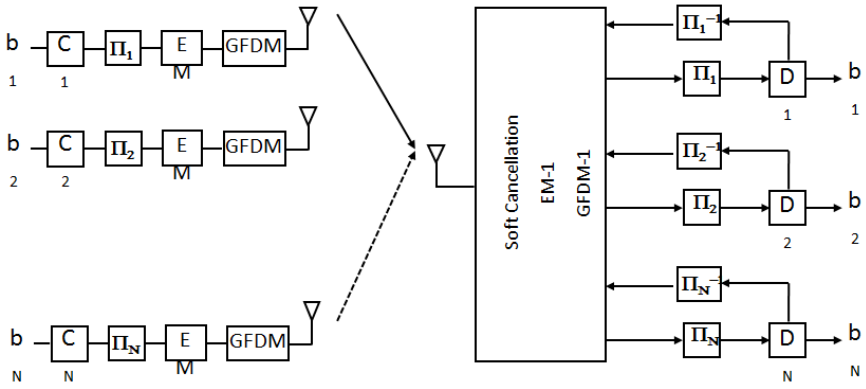

Figure 2.28: Block diagram of proposed combination of GFDM and IDMA.

2.3 Combination of GFDM and IDMA

In the previous section it was shown that both GFDM and IDMA provide advantages for RESCUE scenarios. Therefore it is a natural consideration, to combine GFDM with IDMA to yield a superior system that takes advantages of both components. In GFDM we emphasize the flexibility to adapt to many different channel conditions and the possibility to coexist with other wireless systems because of its very low OOB radiation. From IDMA we appreciate the possibility of simultaneous transmission of every all users at the same frequencys, which can significantly reduce scheduling overhead. Furthermore, the combination of GFDM with IDMA would result in a completely non-orthogonal system which can exploit all the benfits of non-orthogonality in aspects of both waveform properties and multiple access.

Fig. 2.28 shows the proposed block diagram of the combination of GFDM and IDMA. At the transmitter side, each user distributes its encoded bits and extended mapped symbols onto the full allocated time-frequency grid of the GFDM block. Then a CP is added and each user transmits its signal over the wireless channel to the receiver. Then, at the receiver, either SUD or MUD can be carried out. SUD is easily achieved by synchronizing to the user of interest, and performing the IDMA-SUD with an extra step of considering the GFDM modulation in the extended demapper. For MUD the receiver is required to perform the soft-cancellation between the users either in the data domain after GFDM demodulation or directly onto the received antenna signal.

There exist two ideas on how GFDM can be configured as the underlying waveform to best serve IDMA. One is to allocate the entire bandwidth and subsymbols to each user so that the data of each user is distributed over the entire bandwidth that is available. Another approach is to group the available bandwidth into smaller channels, each containing one wide subcarrier. Then, on each subcarrier GFDM is configured to act as a single-carrier system where the interleaved bits are transmitted as in the standard configuration. This way initial decoupling of users is achieved by separating in frequency, but spectral efficiency is kept high due to IDMA on each single carrier. For example, different subcarriers can be used for different purposes, such as source, relay and feedback transmissions.

In general, research on the combination of IDMA and GFDM is ongoing and no detailed results are available by the time of this writing. More results are to be researched for inclusion into the final report on multiple access in D1.3.

3. Reduced-Complexity Multi-Relay Coordinated MIMO Beamforming Technique

Frequency reuse has a potential of enhancing the network coverage and accommodating more users in a specific communication area. However, such reuse may produce severe co-channel interference especially when the network is dense. In order to handle such problem, multi-relay coordinated multiple-input multiple-output (MIMO) beamforming techniques have potential of enhancing the spectrum efficiency and guaranteeing the reliability of unpredictable wireless communication environments, which fits to the perspective of RESCUE project.

3.1 Motivation and Objective

In this chapter, a reduced-complexity multi-relay coordinated MIMO beamforming technique is considered in order to efficiently handle the co-channel interference and increase the system performances. Comparing with multi-relay cooperative MIMO beamforming technique that requires the data-level sharing among relay stations (RSs) [LJ08], multi-relay coordinated MIMO beamforming allows each user to be served by one specific relay station (RS) whereas the set of precoders to be optimized jointly among RSs. In this case, only the transmitter-side CSI is shared by RSs, which significantly reduces the backhaul burden among RSs.

In the literature, there are many ways to handle the coordinated MIMO beamforming problems. For example, in [DY10], Lagrangian duality theory was adopted to solve the weighted sum-power minimization problem with SINR constraints. In [HZB+12], the relation between the SINR optimization and the power optimization has been applied to achieve a distributed solution of maximization of the minimum SINR (max-min SINR) problem under sum-power constraint, where solving the max-min SINR problem provides a better rate-fairness particularly important for the cell-edge users. Meanwhile, a robust max-min SINR problem under per-RS power constraints was proposed by Tajer et al. in [TPW11; HZB+12]. With the transmit CSI to be shared by RSs, it is shown that Tajer et al.'s algorithm leads to the optimal solution of the max-min SINR problem. However, the optimal solution is carried out by alternatively solving a standard semidefinite programs (SDP) problem in conjunction with a linear bi-section search, where the SDP is performed over matrices with more degrees of freedom than beamforming vectors, so that the solution comes with relatively high computational complexity [SB04]. Motivated by this observation, the objective of this work is to propose a reduced-complexity multi-relay coordinated MIMO beamforming for solving the max-min SINR problem under per-RS power constraints. Comparing with the optimum solution, the proposed algorithm can exhibit close performance with faster convergence and lower computational complexity.

3.2 System Model and Problem Formulation

Consider that there is a central BS broadcasting different set of data streams to L RSs, where each of RSs accommodated with M transmit antennas serves K single-antenna based users. In this case, all the nodes are operated in the same frequency band with flat fading channels. Assume that only the transmit CSIs are shared between RSs but no data sharing, hence, the discrete-time equivalent form of received signal at the kth user served by the jth RS is given by

$$\mathrm{y}_{(j,k)} = \sum_{l=1}^{L} \mathbf{h}_{(j,k),l}^{T} \mathbf{x}_l + \mathrm{v}_{(j,k)}, \ j=1,\ldots,L, k=1,\ldots,K, \tag{3.1}$$

where $\mathbf{x}_l$ denotes an $M \times 1$ signal vector transmitted by the lth RS; $\mathbf{h}_{(j,k),l}$ denotes an $M \times 1$ channel transition vector between the lth RS and the (j,k)th user; v denotes the additive white Gaussian noise with zero mean and variance σ_{v}^2; and $(\cdot)^T$ denotes the matrix transpose. The lth RS employs an $M \times K$ ($K \leq M$) precoding matrix $\mathbf{T}_l$ to relate $\mathbf{x}_l$ to a $K \times 1$ symbol vector $\mathbf{s}_l$

$$\mathbf{x}_l = \mathbf{T}_l \mathbf{s}_l, \tag{3.2}$$

where the kth element of $\mathbf{s}_l$, denoted by $\mathrm{s}_{(l,k)}$, is the symbol transmitted to the kth user served by the lth RS.

The (j,k)th user decodes the corresponding message $\mathrm{s}_{(j,k)}$ with the interferences to be treated as noise. The SINR

of the jth RS to the (j,k)th user link is

$$\mathrm{SINR}_{(j,k)} = \frac{p_{k,j}|\mathbf{h}_{(j,k),j}^T \mathbf{t}_{k,j}|^2}{\mathscr{I}_{(j,k),j} + \mathscr{I}_{(j,k),l} + \sigma_{\mathrm{v}}^2}, \tag{3.3}$$

where $\sqrt{p_{k,j}}$ times $\mathbf{t}_{k,j}$ denotes the kth column of the precoding matrix $\mathbf{T}_j$, $\mathbf{t}_{k,j}$ is the beamforming vector with unity norm, and $p_{k,j}$ represents the transmit-power spent on the kth symbol $\mathrm{s}_{(j,k)}$; $\mathscr{I}_{(j,k),j}$ and $\mathscr{I}_{(j,k),l}$ denote the intra-cell interference and inter-cell interference, respectively, with their mathematical form given by

$$\mathscr{I}_{(j,k),j} = \sum_{n \neq k} p_{n,j} |\mathbf{h}_{(j,k),j}^T \mathbf{t}_{n,j}|^2, \tag{3.4}$$

$$\mathscr{I}_{(j,k),l} = \sum_{l \neq j} \|\mathbf{h}_{(j,k),l}^T \mathbf{T}_l\|^2 \tag{3.5}$$

with $\|\cdot\|$ denotes the Frobenius norm.

Based on the above system description, the max-min SINR problem can be mathematically described by

$$\begin{aligned} \max_{\mathbf{T}_j} \min_{j,k} \quad & \mathrm{SINR}_{(j,k)} / \overline{\gamma}_{(j,k)} \\ \text{s.t.} \quad & \|\mathbf{T}_j\|^2 \leq \overline{P}_j, \forall j, \end{aligned} \tag{3.6}$$

where $\overline{\gamma}_{(j,k)}$ denotes the target SINR for the (j,k)th user, $\overline{P}_j$ is the power constraint for the jth RS. With the transmit CSI to be shared by RSs, each RS can run the optimization algorithms (such as the bi-section search algorithm in [TPW11]) independently and form the same beamforming solutions for all RSs. It is worthwhile to note that although the computational complexity is not a considerable issue for large RSs, in practice, low-complex algorithms are needed for low-cost access points such as MIMO relays for dense network.

3.3 Reduced-complexity Bi-Layer Iterative Algorithm

The proposed reduced-complexity bi-layer iterative algorithm can be divided into inner layer search and outer layer search: In the inner layer search, the uplink-downlink duality theory is used to address the optimization of the max-min SINR problem under a predetermined sum-power constraint; While in the outer layer search, the optimal downlink transmit-power vector, which was obtained from the inner layer, is proportionally scaled to satisfy per-RS power constraints.

3.3.1 Bi-layer Iterative Algorithm Design

In detail, the optimization problem solved by the inner layer process can be expressed as

$$\begin{aligned} \max_{\mathbf{T}_j} \min_{j,k} \quad & \mathrm{SINR}_{(j,k)} / \overline{\gamma}_{(j,k)} \\ \text{s.t.} \quad & \textstyle\sum_{j=1}^{L} \|\mathbf{T}_j\|^2 \leq \overline{P}_{\mathrm{sum}}, \end{aligned} \tag{3.7}$$

where $\overline{P}_{\mathrm{sum}}$ is defined as the predetermined sum-power constraint. Such problem can be solved based on the standard uplink-downlink duality theory. Specifically, start from that the L RSs compose a virtual RS serving LK users, and the precoding matrix of the virtual RS formulates a block-diagonal structure, where the jth element on the block-diagonal is $\mathbf{T}_j$. Such block-diagonal structure limits the job within the coordinated beamforming. Denote that $\mathbf{q}_j = \left[q_{1,j}, \ldots, q_{K,j}\right]^T$ is the virtual uplink transmit-power vector for the users served by the jth RS, the virtual uplink SINR for the kth user served by the jth RS is given by

$$\mathrm{SINR}_{(j,k)}^{\mathrm{UL}} = \frac{q_{k,j} \left|\mathbf{h}_{(j,k),j}^T \mathbf{t}_{k,j}\right|^2}{\mathscr{I}_{(j,k),j}^{\mathrm{UL}} + \mathscr{I}_{(j,k),l}^{\mathrm{UL}} + \sigma_{\mathrm{v}}^2}, \tag{3.8}$$

where

$$\mathscr{I}_{(j,k),j}^{\mathrm{UL}} = \sum_{n \neq k} q_{n,j} \left|\mathbf{h}_{(j,k),j}^T \mathbf{t}_{k,j}\right|^2, \tag{3.9}$$

$$\mathscr{I}^{\mathrm{UL}}_{(j,k),l} = \sum_{l \neq j,n} q_{n,l} \left| \mathbf{h}^T_{(l,n),j} \mathbf{t}_{k,j} \right|^2 . \tag{3.10}$$

Under the sum-power constraint, as shown in in [SB04], the uplink and downlink problems share the same SINR achievable region, which means that, despite the block-diagonal structure of the precoding matrix, the downlink max-min SINR problem under sum-power constraint can be solved via the virtual uplink max-min SINR problem under the same sum-power constraint. In this case, the joint beamforming and power allocation algorithm in [SB04] can be implemented in order to get the optimal solution. Meanwhile, the problem can also be solved with a distributed manner as shown in [HZB+12].

Following the optimal beamforming vectors $\mathbf{t}_{k,j}, \forall k, j$, formulation, the optimal downlink transmit-power vector (denoted by $\breve{\mathbf{p}}$) can be formulated by finding the first LK elements of the dominant eigenvector of the matrix

$$\mathbf{D} \triangleq \begin{bmatrix} \mathbf{C}\boldsymbol{\psi} & \mathbf{C}\mathbf{u} \\ \frac{1}{\overline{P}_{\mathrm{sum}}} \mathbf{1}^T \mathbf{C}\boldsymbol{\psi} & \frac{1}{\overline{P}_{\mathrm{sum}}} \mathbf{1}^T \mathbf{C}\mathbf{u} \end{bmatrix}, \tag{3.11}$$

which can be scaled so that its last element equals one [SB04]. Regarding to the matrix $\mathbf{D}$,

$$\mathbf{C} = \mathrm{diag} \left\{ \frac{\overline{\gamma}_{(1,1)}}{\left| \mathbf{h}^T_{(1,1),1} \mathbf{t}_{1,1} \right|^2}, \ldots, \frac{\overline{\gamma}_{(L,K)}}{\left| \mathbf{h}^T_{(L,K),L} \mathbf{t}_{K,L} \right|^2} \right\}; \tag{3.12}$$

$\mathbf{u} = \left[\sigma_{\mathrm{v}}^2, \ldots, \sigma_{\mathrm{v}}^2 \right]^T$ is $LK \times 1$ noise vector; $\mathbf{1}$ is all-one vector with the size of $LK \times 1$; $\boldsymbol{\psi}$ consists of $LK \times LK$ sub-matrices $\boldsymbol{\psi}_{j,l}, \forall j, l$, with the size of $K \times K$ each, and the (m,n)-th element of each sub-matrix is defined as:

$$\boldsymbol{\psi}^{(m,n)}_{j,l} = \begin{cases} 0, & l = j \text{ and } n = m, \\ \left| \mathbf{h}^T_{(j,m),l} \mathbf{t}_{n,l} \right|^2, & \text{otherwise.} \end{cases} \tag{3.13}$$

Hence, the downlink transmit-power vector $\breve{\mathbf{p}}$ is formed by

$$\breve{\mathbf{p}} = \left[\mathbf{p}_1^T, \ldots, \mathbf{p}_L^T \right]^T, \tag{3.14}$$

where $\mathbf{p}_j = \left[p_{1,j}, \ldots, p_{K,j} \right]^T$ is the transmit-power vector for the jth RS, $\sum_{j=1}^{L} \left\| \mathbf{p}_j \right\|_1 = \overline{P}_{\mathrm{sum}}$, and $\| \cdot \|_1$ stands for the Manhattan norm of a vector.

After we found the initial beamforming vectors through the inner layer process, the outer layer process is used to satisfy the current stage per-RS power constraints. Let the superscript (n) denote the nth iteration of bi-layer iterative algorithm, and let $\breve{\mathbf{p}}^{(n)}$ denote the tentative downlink transmit-power vector obtained from the inner layer process. By implementing the proposed *Proposition 1*, $\breve{\mathbf{p}}^{(n)}$ can be proportionally scaled for satisfying the per-RS power constraints, and the updated $\overline{P}^{(n+1)}_{\mathrm{sum}}$ will be used as the sum-power constraint for the next time inner layer process.

Proposition 1: After giving the optimal downlink transmit-power vector $\breve{\mathbf{p}}$ for the max-min SINR problem under sum-power $\overline{P}_{\mathrm{sum}}$ constraint, each element in $\breve{\mathbf{p}}$ is continuous and strictly monotonically increasing with respect to $\overline{P}_{\mathrm{sum}}$.

Proof: Fixed the set of beamforming vectors $\mathbf{t}_{k,j}, \forall j, k$, let $\widetilde{\mathbf{p}} \triangleq \left[\breve{\mathbf{p}}^T 1 \right]^T$ denote an extended power vector. As we mentioned above, the way of finding the optimal downlink transmit-power vector $\breve{\mathbf{p}}$ can be formulated as

$$\begin{bmatrix} \mathbf{C}\boldsymbol{\psi} & \mathbf{C}\mathbf{u} \\ \frac{1}{\overline{P}_{\mathrm{sum}}} \mathbf{1}^T \mathbf{C}\boldsymbol{\psi} & \frac{1}{\overline{P}_{\mathrm{sum}}} \mathbf{1}^T \mathbf{C}\mathbf{u} \end{bmatrix} \widetilde{\mathbf{p}} = \lambda_{\max} \widetilde{\mathbf{p}}, \tag{3.15}$$

where $\lambda_{\max}$ is the dominant eigenvalue, and then we have

$$\left(\begin{bmatrix} \mathbf{C}\boldsymbol{\psi} & \mathbf{C}\mathbf{u} \\ \frac{1}{\overline{P}_{\mathrm{sum}}} \mathbf{1}^T \mathbf{C}\boldsymbol{\psi} & \frac{1}{\overline{P}_{\mathrm{sum}}} \mathbf{1}^T \mathbf{C}\mathbf{u} \end{bmatrix} - \lambda_{\max} \mathbf{I} \right) \widetilde{\mathbf{p}} = \mathbf{0}, \tag{3.16}$$

Algorithm 1: Bi-Layer Iterative Algorithm

1) Initialize $\overline{P}_{\text{sum}}^{(1)} = \sum_{j=1}^{L} \overline{P}_j$, an arbitrary set of $\mathbf{t}_{k,j}^{(1)}, \forall k, j$, and $n = 0$;
2) Let $n = n+1$, solve the max-min SINR problem under the sum-power $\overline{P}_{\text{sum}}^{(n)}$ constraint from [SB04] or [HZB+12] and obtain $\breve{\mathbf{p}}^{(n)}$;
3) **If** $\max_j \|\mathbf{p}_j^{(n)}\|_1/\overline{P}_j,\ j \in [1,L]$, is greater than one, scale $\breve{\mathbf{p}}^{(n)}$ with a scalar α_1, where $(0 < \alpha_1 < 1)$, to make $\max_j \|\mathbf{p}_j^{(n)}\|_1/\overline{P}_j = 1$, $j \in [1,L]$. Set $\overline{P}_{\text{sum}}^{(n+1)} = \left\|\alpha_1 \breve{\mathbf{p}}^{(n)}\right\|_1$;
4) **Elseif** $\max_j \|\mathbf{p}_j^{(n)}\|_1/\overline{P}_j,\ j \in [1,L]$, is smaller than one, scale $\breve{\mathbf{p}}^{(n)}$ with a scalar α_2, where $(\alpha_2 > 1)$, to make $\max_j \|\mathbf{p}_j^{(n)}\|_1/\overline{P}_j = 1$, $j \in [1,L]$. Set $\overline{P}_{\text{sum}}^{(n+1)} = \left\|\alpha_2 \breve{\mathbf{p}}^{(n)}\right\|_1$;
5) Repeat steps $2)-4)$ until $\left|\overline{P}_{\text{sum}}^{(n+1)} - \overline{P}_{\text{sum}}^{(n)}\right| < \varepsilon$.

where $\mathbf{I}$ is $(LK+1)\times(LK+1)$ identity matrix, and $\mathbf{0}$ denotes all-zero vector with the size of $(LK+1)\times 1$. Following, we further derive (3.16) to an equation consisted of $\overline{P}_{\text{sum}}$ and $\breve{\mathbf{p}}$, which is

$$\frac{1}{\overline{P}_{\text{sum}}}\mathbf{1}^T\mathbf{C}\psi\breve{\mathbf{p}} + \frac{1}{\overline{P}_{\text{sum}}}\mathbf{1}^T\mathbf{C}\mathbf{u} = \lambda_{\max}. \tag{3.17}$$

Because that each element of the vector $\mathbf{1}^T\mathbf{C}\psi$ is a positive real value, it is easy to conclude that each element of $\breve{\mathbf{p}}$ is a strictly monotonically increasing function of $\overline{P}_{\text{sum}}$. □

Following *Proposition 1*, the detailed power scaling method can be described as: If $\max_j \|\mathbf{p}_j^{(n)}\|_1/\overline{P}_j,\ j \in [1,L]$, is larger than one, we scale $\breve{\mathbf{p}}^{(n)}$ with a scalar α_1 where $(0 < \alpha_1 < 1)$, and α_1 reaches its maximum when $\max_j \|\mathbf{p}_j^{(n)}\|_1/\overline{P}_j,\ j \in [1,L]$, is back to one, then, update $\overline{P}_{\text{sum}}^{(n+1)} = \left\|\alpha_1 \breve{\mathbf{p}}^{(n)}\right\|_1$; Otherwise, if $\max_j \|\mathbf{p}_j^{(n)}\|_1/\overline{P}_j$, $j \in [1,L]$, is smaller than one, we scale $\breve{\mathbf{p}}^{(n)}$ with a scalar α_2 where $(\alpha_2 > 1)$, and α_2 reaches its minimum when $\max_j \|\mathbf{p}_j^{(n)}\|_1/\overline{P}_j,\ j \in [1,L]$, is reach to one, then, update $\overline{P}_{\text{sum}}^{(n+1)} = \left\|\alpha_2 \breve{\mathbf{p}}^{(n)}\right\|_1$. Finally, if $\left|\overline{P}_{\text{sum}}^{(n+1)} - \overline{P}_{\text{sum}}^{(n)}\right| < \varepsilon$, then the outer iteration is said to have converged and the entire algorithm stopped, where ε is a small positive value very close to zero. To sum up, based on the above analysis, the proposed bi-layer iterative algorithm is given by Algorithm 1, where $\varepsilon = 10^{-6}$, and $\overline{P}_{\text{sum}}^{(1)}$ can be arbitrarily chosen from the range of $(0, \sum_{j=1}^{L} \overline{P}_j]$.

3.3.2 Computational Complexity and Convergence Analysis

The computational complexity of Algorithm 1 can be analysed as follows: For the algorithm in the inner layer, as shown in [SB04], the main complexity in each iteration involves the formulation of ψ, the eigenvalue decomposition of $\mathbf{D}$, and LK times generalized eigenvalue decomposition of a matrix pair with the size of $\mathscr{R}^{M\times M}$, where, if L is selected from a small integer, their worst-case complexity are $\mathscr{O}\{MK^2\}$, $\mathscr{O}\{K^3\}$ and $\mathscr{O}\{M^3K\}$, respectively. Assume that $K = M$ and N_{in} represents the number of iterations for the algorithm, the overall worst-case inner layer complexity is $\mathscr{O}\{N_{\text{in}}M^4\}$. For the outer layer process, the complexity just involves certain element-wise multiplications and additions of $\breve{\mathbf{p}}$, which can be ignored by comparing with M^4. Then the whole computational complexity of the proposed algorithm is $\mathscr{O}\{N_{\text{out}}N_{\text{in}}M^4\}$, where N_{out} denotes the number of iterations for the outer loop. In comparison, the optimal solution (cf. [TPW11]) of the problem (3.6) involves the bi-section search and iteratively solving a set of SDP problems. In this case, referring to [LY06], the whole computational complexity is $\mathscr{O}\{\log(a_{\max})\log(1/\varepsilon)M^{6.5}\}$, where $a_{\max}$ is the upper-limit of the bisection search.

For the convergence analysis of the proposed algorithm, the convergence property of the inner layer process has been well investigated in Section IV.A of [SB04]. Here, we mainly focus on analyzing the convergence of the outer layer process. According to *Proposition 1*, with the strictly monotonic property between $\overline{P}_{\text{sum}}$ and $\breve{\mathbf{p}}$, the proposed algorithm iteratively scales the downlink transmit-power vector $\breve{\mathbf{p}}^{(n)}$, and terminates at the point $\breve{\mathbf{p}}^{(*)}$. The stopping condition is: $\max_j \|\mathbf{p}_j^{(*)}\|_1/\overline{P}_j = 1$, $j \in [1,L]$ after the n^{th} inner layer process. In this case, further iterations would not change the transmit-power vector $\breve{\mathbf{p}}$, i.e., we have $\|\breve{\mathbf{p}}^{(n+1)}\|_1 = \|\breve{\mathbf{p}}^{(n)}\|_1$ (or equivalently $|\overline{P}_{\text{sum}}^{(n+1)} - \overline{P}_{\text{sum}}^{(n)}| = 0$). The convergence is therefore proved.

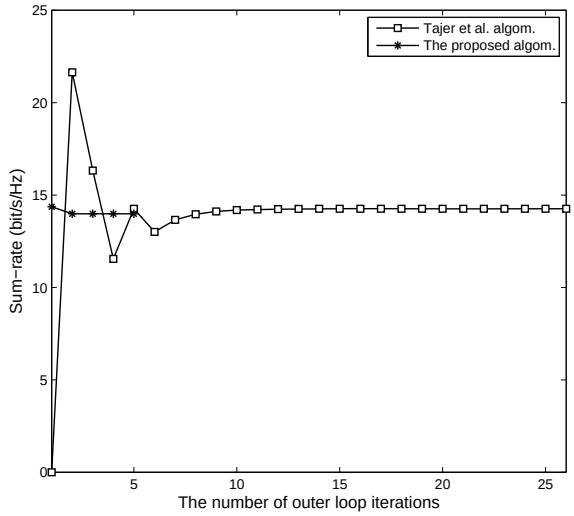

Figure 3.1: The sum-rate performance vs. the number of outer loop iterations, where $\overline{P}_1 = \overline{P}_2 = 40\text{dBm}$ (normalized by noise) [HMY+14].

3.4 Numerical Results

In this section, we investigated the performance of the proposed reduced-complexity coordinated beamforming by comparing with two baselines. The first one is the joint beamforming and power allocation algorithm in [TPW11], which led to the optimal solution of the problem (3.6); The second one is the algorithm for solving max-min SINR problem under sum-power constraint (e.g., see [SB04; HZB+12]). Throughout the entire experiments, all channels were generated as independent Rayleigh fading, which remained static over the transmission of each block. The variances of inter-cell channel links were configured as 0.1 so that the coordinated network was possible to be considered as weak cross-talk interference. Assumed that there were $L = 2$ RSs, and each of them was equipped with $M = 4$ antennas and served $K = 3$ users. 3 was set up as the target SINR per active user (i.e., 2 bit/s/Hz per active user). The SNR was defined as the target transmit-power normalized by noise ratio.

Experiment 1: The objective of this experiment was to examine the convergence behaviors and the rate performance of the proposed bi-layer iterative algorithm. Fig. 3.1 illustrated the convergence behaviors of the proposed algorithm and Tajer et al.'s algorithm in [TPW11] for a random channel realization. The results showed that the proposed algorithm only needed around 3 outer loop iterations to reach the stable point, which revealed faster convergence by comparing with Tajer et al.'s algorithm. Fig. 3.2 illustrated the sum-rate performance and power consumption for different algorithms. As shown in Fig. 3.2 (a), the proposed algorithm achieves very close sum-rate performance to Tajer et al.'s algorithm. For the probability of power consumption, as shown in Fig. 3.2 (b), one RS's power constraint indeed satisfied with equality. In this case, we normalized the actual transmit-power by the target transmit-power. Moreover, in order to highlight the algorithm that solves the max-min SINR problem under sum-power constraint had more flexibility for power allocation, we limited $\overline{P}_1 = 0.1 \times \text{SNR}$ and $\overline{P}_2 = 1.9 \times \text{SNR}$.

Experiment 2: Mathematically, unlike the power minimization problem, the problem (3.6) can always lead to a solution. However, by formulating the actual SINRs, if the ratios $\text{SINR}_{(j,k)}/\overline{\gamma}_{(j,k)}$ for all active users were less than one, the user switch-off strategies should be implemented to guarantee all active users' target SINRs. Hence, in this experiment, we aim to examine the different user switch-off strategies to guarantee all active users' target SINRs. There are several user switch-off strategies being examined: 1) switching off the user with the largest received interference power; 2) switching off the user with the smallest received signal power; 3) switching off the user with the smallest signal to signal to leakage plus noise ratio (SLNR); 4) switching off the user with the largest leakage interference power. As shown in Fig. 3.3, switching off the user with the lowest received signal power strategy can always lead to a better performance by comparing with other strategies.

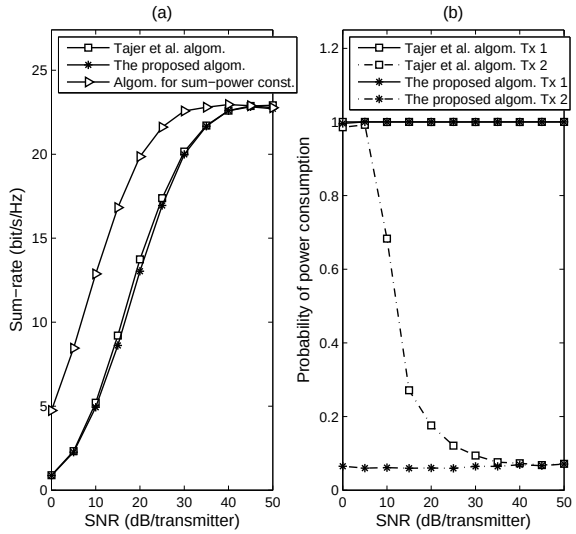

Figure 3.2: **(a) The sum-rate vs. SNR; (b) The probability of power consumption vs. SNR. For both (a) and (b), assume that $\overline{P}_1 = 0.1 \times \mathrm{SNR}$ and $\overline{P}_2 = 1.9 \times \mathrm{SNR}$ [HMY+14].**

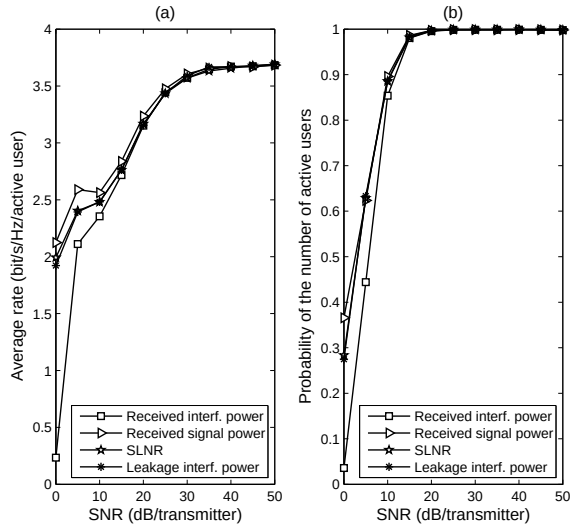

Figure 3.3: **(a) The sum-rate vs. average rate; (b) The probability of the number of active users vs. SNR. For both (a) and (b), assume that $\overline{P}_1 = 1 \times \mathrm{SNR}$ and $\overline{P}_2 = 1 \times \mathrm{SNR}$ [HMY+14].**

4. Conclusion

This document described the current research status of RESCUE regarding multiple access and multi-antenna technologies. After a summary of the requirements on the employed waveforms and MA schemes for RESCUE scenarios, CSMA/CA was introduced in detail. The technique and rationale behind CSMA/CA was presented and it was stated that CSMA/CA is used as the MA scheme used for the demonstrator implementation in WP3. Apart from CSMA/CA, novel MA schemes are investigated in WP1.

GFDM was shown to be in particular suitable for the scenarios that are targeted by RESCUE applications. Its robustness against asynchronicity provides means to efficiently cope with non-synchronized access and misalignments. It was shown, that GFDM can easily work together with CSMA/CA to provide a robust PHY scheme for P2P transmissions. Several investigations have shown that GFDM can outperform the wide-spread OFDM system in both orthogonal and synchronized and non-synchronized access. A method was presented that exploits the block structure of GFDM to achieve transmit diversity regardless of the non-orthogonality of the underlying GFDM waveform. The scheme was shown to outperform GFDM in a fading multipath environment. Furthermore, when non-synchronized access in GFDM occurs, a simple yet effective method to estimate and compensate time and frequency misalignment has been presented and its performance was evaluated.

Moreover, the non-orthogonal multiple access scheme IDMA was presented. With IDMA, all users transmit at the same time-frequency resource and can only be distinguished by their respective interleaver. IDMA employs low code rates per user, however the system's spectral efficiency can be raised above the capacity that is achievable by orthogonal MA schemes such as TDMA. Two detection modes are available for this scheme. In SUD, only one user is decoded at a time, and the signal from other users is just considered as noise. In this situation, the low code rates of the users help to operate in very low SINR regions. For SUD the decoding complexity is very low since only a single data stream is to be detected. SUD can be efficiently applied in unpredictable environments, where the SNR is often very low. As a second operation mode, IDMA offers MUD, where the decoder jointly detects all transmitting users at the same time. This is achieved by using decoded information from all users to apply soft-cancellation at the receiver to decode a better estimate of the transmitted sequences. Then, iterations are carried out to finally decouple all users. This operation mode is more complex, however its achievable rates are above the rates of orthogonal MA schemes.

We have shown an algorithm with reduced complexity to solve the max-min SINR problem with per-RS power constraints. This algorithm distributes transmit power among several relay stations to achieve optimal performance in multi-relay coordinated beamforming scenarios to provide a fair distribution rates per user. It was shown that the proposed algorithm can reach the same performance as previous works, however, with a significantly reduced computational complexity as the iterations converge faster. Numerical evidence was provided to ensure the correctness of the proposed algorithm.

This deliverable provides the baseline for further research in RESCUE regarding multiple access und multi-antenna techniques. In future work, more aspects on the combination of GFDM and IDMA are to be investigated and the benefits shall be analyzed. Additionally, spatial multiplexing for GFDM will be analyzed in terms of spectral efficiency and robustness in the unpredictable environments of RESCUE.

5. References

[AI07] G. Acosta-Marum and M.A. Ingram. “Six time- and frequency- selective empirical channel models for vehicular wireless LANs”. In: *IEEE Vehicular Technology Magazine* 2.4 (Dec. 2007), pp. 4–11. ISSN: 1556-6072.

[AKE08] A. Awoseyila, C. Kasparis, and B. G. Evans. “Improved Preamble-Aided Timing Estimation for OFDM Systems”. In: *IEEE Communications Letters* 12.11 (Nov. 2008), pp. 825–827.

[Ala98] S.M. Alamouti. “A Simple Transmit Diversity Technique for Wireless Communications”. In: *IEEE Journal on Selected Areas in Communications* 16.8 (Oct. 1998), pp. 1451–1458.

[AlD01] N. Al-Dhahir. “Single-Carrier Frequency-Domain Equalization for Space-Time Block-Coded Transmissions over Frequency-Selective Fading Channels”. In: *IEEE Communications Letters* 5.7 (July 2001), pp. 304–306.

[AM11] K. Anwar and T. Matsumoto. “Very Simple BICM-ID Using Repetition Code and Extended Mapping with Doped Accumulator”. In: *Wireless Personal Communications, Springer* (Sept. 2011). doi:10.1007/s11277-011-0397-1.

[AM13] K. Anwar and T. Matsumoto. “Field Measurement Data-based Performance Evaluation for Slepian-Wolf Relaying Systems”. In: *IEICE General Conference 2013*. Gifu, Japan, Mar. 2013.

[Bin90] J.A.C. Bingham. “Multicarrier Modulation for Data Transmission: An Idea Whose Time Has Come”. In: *IEEE Communications Magazine* 28.5 (May 1990), pp. 5–14.

[Bri01] S. ten Brink. “Convergence behavior of iteratively decoded parallel concatenated codes”. In: *IEEE Transactions on Communications* 49.10 (Oct. 2001), pp. 1727–1737.

[D11] The RESCUE Team. *D1.1 - System Scenarios and Technical Requirements*. Tech. rep. The RESCUE Institution, 2014.

[DDT09] Mathilde Durvy, Olivier Dousse, and Patrick Thiran. “Self-Organization Properties of CSMA/CA Systems and Their Consequences on Fairness”. In: *IEEE Transactions on Information Theory* 55.3 (Mar. 2009), pp. 931–943. ISSN: 0018-9448.

[DGK+13] Panagiotis Demestichas, Andreas Georgakopoulos, Dimitrios Karvounas, Kostas Tsagkaris, Vera Stavroulaki, Jianmin Lu, Chunshan Xiong, and Jing Yao. “5G on the Horizon: Key Challenges for the Radio-Access Network”. In: *IEEE Vehicular Technology Magazine* 8.3 (Sept. 2013), pp. 47–53. ISSN: 1556-6072.

[DY10] H. Dahrouj and W. Yu. “Coordinated Beamforming for the Multicell Multi-Antenna Wireless System”. In: *IEEE Trans. Wireless Commun.* 9.5 (May 2010), pp. 1748–1759.

[DYF+14] Zhiguo Ding, Zheng Yang, Pingzhi Fan, and H. Vincent Poor. “On the Performance of Non-Orthogonal Multiple Access in 5G Systems with Randomly Deployed Users”. In: *IEEE Signal Processing Letters* 21.12 (Dec. 2014), pp. 1501–1505. ISSN: 1070-9908.

[FA14] Gerhard Fettweis and Siavash Alamouti. “5G: Personal Mobile Internet Beyond What Cellular Did to Telephony”. In: *IEEE Communications Magazine* 52.2 (Feb. 2014), pp. 140–145.

[Fet14] Gerhard P. Fettweis. “The Tactile Internet: Applications and Challenges”. In: *IEEE Vehicular Technology Magazine* 9.1 (Mar. 2014), pp. 64–70.

[FOO00] P. Frenger, P. Orten, and T. Ottosson. “Code-spread CDMA using maximum free distance low-rate convolutional codes”. In: *IEEE Transactions on Communications* 48. 1 (Jan. 2000), pp. 135–144.

[FOT+12] K. Fukawa, S. Ormsub, A. Tolli, K. Anwar, and T. Matsumoto. “EXIT-constrained BICM-ID Design using Extended Mapping”. In: *EURASIP Journal on Wireless Commun. and Networking* 2012. 1 (Feb. 2012).

[Hag04] J. Hagenauer. “The EXIT Chart - Introduction to extrinsic information transfer in iterative processing”. In: *12th European Signal Processing Conference (EUSIPCO)*. Vienna, Austria, Sept. 2004, pp. 1541–1548.

[HHS+09] Hojoong Kwon, Hanbyul Seo, Seonwook Kim, and Byeong Gi Lee. “Generalized CSMA/CA for OFDMA systems: protocol design, throughput analysis, and implementation issues”. In: *IEEE Transactions on Wireless Communications* 8.8 (Aug. 2009), pp. 4176–4187. ISSN: 1536-1276.

[HMY+14] Jiancao Hou, Yi Ma, Na Yi, and Rahim Tafazolli. “Reduced-Complexity Coordinated Beamforming for Multicell Downlink Max–Min SINR Problem”. In: *IEEE Wireless Communications Letters* 3.4 (Aug. 2014), pp. 353–356. ISSN: 2162-2337.

[HS06] P. A. Hoeher and H. Schoeneich. “Interleave-division multiple access from a multiuser point of view”. In: *5-th Int. Symp. Turbo Codes Related Topics Connection 6th Int. ITG-Conf. Source Channel Coding*. Germany, Apr. 2006, pp. 140–144.

[HZB+12] Y. Huang, G. Zheng, M. Bengtsson, K-K. Wong, L. Yang, and B. Ottersten. “Distributed multicell beamforming design approaching Pareto boundary with max-min fairness”. In: *IEEE Trans. Wireless Commun.* 11.8 (Aug. 2012), pp. 2921–2933.

[IVS+10] Tero Ihalainen, Ari Viholainen, Tobias Hidalgo Stitz, and Markku Renfors. “Generation of Filter Bank-Based Multicarrier Waveform Using Partial Synthesis and Time Domain Interpolation”. In: *IEEE Transactions on Circuits and Systems I: Regular Papers* 57.7 (July 2010), pp. 1767–1778. ISSN: 1549-8328.

[KBU09] K. Kusume, G. Bauch, and W. Utschick. “IDMA vs. CDMA: detectors, performance and complexity”. In: *IEEE Global Telecommunications Conference (GLOBECOM 2009)*. Hawaii, USA, Nov. 2009, pp. 1–8.

[KWJ+14] Martin Kasparick, Gerhard Wunder, Peter Jung, and Dick Maryopi. *Bi-orthogonal Waveforms for 5G Random Access with Short Message Support*. 2014.

[Kyö07] Kyösti. *IST-WINNER D1.1.2: WINNER II Channel Models*. Tech. rep. 2007.

[LJ08] E. Larsson and E. Jorswieck. “Competition versus cooperation on the MISO interference channel”. In: *IEEE J. Sel. Areas Commun.* 26.7 (Sept. 2008), pp. 1059–1069.

[LLW+06] P. Li, L. Liu, K. Wu, and W. K. Leung. “Interleave division multiple access”. In: *IEEE Transactions on Wireless Communications* 5. 4 (Apr. 2006), pp. 938–947.

[LW00] K.F. Lee and D.B. Williams. “A Space-Time Coded Transmitter Diversity Technique for Frequency Selective Fading Channels”. In: *Proceedings IEEE Sensor Array and Multichannel Signal Processing Workshop (SAM’00)*. Cambridge, MA, USA, Aug. 2000, pp. 149–152.

[LY06] Z. Luo and W. Yu. “An Introduction to Convex Optimization for Communications and Signal Processing”. In: *IEEE J. Sel. Areas Commun.* 24.8 (Aug. 2006), pp. 1426–1438.

[MKL+12] N. Michailow, S. Krone, M. Lentmaier, and G. Fettweis. “Bit Error Rate Performance of Generalized Frequency Division Multiplexing”. In: *Proceedings 76th IEEE Vehicular Technology Conference (VTC Fall’12)*. QuÃ©bec City, Canada, Sept. 2012, pp. 1–5.

[MMF14a] Maximilian Matthé, Luciano Leonel Mendes, and Gerhard Fettweis. “GFDM in a Gabor Transform Setting”. In: *IEEE Communications Letters* (2014).

[MMF14b] Maximilian Matthé, Luciano Leonel Mendes, and Gerhard Fettweis. “Space-Time Coding for Generalized Frequency Division Multiplexing”. In: *European Wireless 2014 (EW2014)*. Barcelona, Spain, 2014.

[MMF15] Maximilian Matthé, Luciano Leonel Mendes, and Gerhard P. Fettweis. “Asynchronous Multi-User Uplink Transmission with Generalized Frequency Division Multiplexing”. In: *International Workshop on Advanced PHY and MAC Techniques for Super Dense Wireless Networks (IWSDN) in Conjunction with ICC; submitted*. 2015.

[MMG+14a] Maximilian Matthé, Nicola Michailow, Ivan Gaspar, and Gerhard Fettweis. “Influence of Pulse Shaping on Bit Error Rate Performance and Out of Band Radiation of Generalized Frequency Division Multiplexing”. In: *ICC’14 - Workshop on 5G Technologies (ICC’14 WS - 5G)*. Sydney, Australia, 2014, pp. 43–48.

[MMG+14b] Nicola Michailow, Maximilian Matthé, Ivan Gaspar, A Navarro Caldevilla, Luciano Leonel Mendes, Andreas Festag, and Gerhard Fettweis. “Generalized Frequency Division Multiplexing for 5th Generation Cellular Networks”. In: *IEEE Transactions on Communications* 99 (2014).

[MZB00] H. Minn, M. Zeng, and V.K. Bhargava. “On Timing Offset Estimation for OFDM Systems”. In: *IEEE Communications Letters* 4.7 (July 2000), pp. 242–244.

[SB04] M. Schubert and H. Boche. “Solution of the Multiuser Downlink Beamforming Problem With Individual SINR Constraints”. In: *IEEE Trans. Veh. Technol.* 53.1 (Jan. 2004), pp. 18–28.

[SC97] T.M. Schmidl and D.C. Cox. “Robust Frequency and Timing Synchronization for OFDM”. In: *IEEE Transactions on Communications* 45.12 (Dec. 1997), pp. 1613–1621.

[SH04] H. Schoeneich and P. A. Hoeher. “Adaptive interleave-division multiple access – A potential air interference for 4G bearer services and wireless LANs”. In: *WOCN*. Muscat, Oman, June 2004, pp. 179–182.

[TM00] Kornel Terplan and Patricia A. Morreale. *The Telecommunications Handbook*. Taylor & Francis, 2000, p. 424. ISBN: 0849331374.

[TPW11] A. Tajer, N. Prasad, and X. Wang. “Robust Linear Precoder Design for Multi-Cell Downlink Transmission”. In: *IEEE Trans. Signal Process.* 59.1 (Jan. 2011), pp. 235–251.

[Ver98] S. Verdu. *Multiuser Detection*. Cambridge University Press, 1998.

[Vit79] Andrew James Viterbi. “Spread Spectrum Communications-Myths and Realities”. In: *IEEE Communications Magazines.* 23. 4 (May 1979).

[WAM14] K. Wu, K. Anwar, and T. Matsumoto. “BICM-ID-based IDMA: Convergence and Rate Region Analyses”. In: *IEICE transactions on communications* E97-B.7 (July 2014), pp. 1483–1492.

[WJK+14] Gerhard Wunder, Peter Jung, Martin Kasparick, Thorsten Wild, Frank Schaich, Yejian Chen, Stephan Brink, Ivan Gaspar, Nicola Michailow, Andreas Festag, Luciano Mendes, Nicolas Cassiau, Dimitri Ktenas, Marcin Dryjanski, Slawomir Pietrzyk, Bertalan Eged, Peter Vago, and Frank Wiedmann. “5GNOW: non-orthogonal, asynchronous waveforms for future mobile applications”. English. In: *IEEE Communications Magazine* 52.2 (Feb. 2014), pp. 97–105. ISSN: 0163-6804.

[WKB+12] Gerhard Wunder, Martin Kasparick, Stephan ten Brink, Frank Schaich, Thorsten Wild, Ivan Gaspar, Eckhard Ohlmer, Stefan Krone, Nicola Michailow, Ainoa Navarro, Gerhard Fettweis, Dimitri Ktenas, Vincent Berg, Marcin Dryjanski, Slawomir Pietrzyk, and Bertalan Eged. “5GNOW: Challenging the LTE Design Paradigms of Orthogonality and Synchronicity”. In: *Mobile and Wireless Communication Systems for 2020 and beyond, Workshop at IEEE VTC 2013 – Spring*. Dec. 2012. arXiv: 1212.4034.

[WSC14] Thorsten Wild, Frank Schaich, and Yejian Chen. “5G air interface design based on Universal Filtered (UF-)OFDM”. In: *2014 19th International Conference on Digital Signal Processing*. IEEE, Aug. 2014, pp. 699–704. ISBN: 978-1-4799-4612-9.

[WXL06] P. Wang, J. Xiao, and P. Li. “Comparison of Orthogonal and Non-Orthogonal Approaches to Future Wireless Cellular Systems”. In: *IEEE Vehicular Technology Magazine* 1.3 (Sept. 2006).